

# MODEL COMPARISON FOR SINGLE PARTICLE TRACKING IN BIOLOGICAL FLUIDS

MARTIN LYSY<sup>\*</sup>, NATESH S. PILLAI<sup>†</sup>, DAVID B. HILL<sup>‡</sup>, M. GREGORY FOREST<sup>‡</sup>,  
JOHN MELLNIK<sup>‡</sup>, PAULA VASQUEZ<sup>§</sup>, SCOTT A. MCKINLEY<sup>¶</sup>

July 21, 2014

**ABSTRACT.** State-of-the-art techniques in particle tracking microscopy provide high-resolution path trajectories for the dynamical analysis of diverse foreign particles in biological fluids. For particles on the order of one micron in diameter, these paths are not generally consistent with simple Brownian motion. Despite an abundance of data confirming these findings, stochastic modeling of the complex particle motion has received comparatively little attention. Yet, prediction beyond experimental time scales – such as first-passage times through biological barriers – is a fundamental scientific objective that requires a careful statistical approach. Even among existing candidate models, few attempts have been made at likelihood-based model comparisons and other quantitative evaluations. In this article, we employ a robust Bayesian methodology to address this gap. We analyze two competing models – fractional Brownian motion (fBM) and a generalized Langevin equation (GLE) consistent with viscoelastic theory – applied to an ensemble of 30 second paths of 1  $\mu\text{m}$  diameter tracer particles in human lung mucus. We conclude that either fBM or a GLE with a long memory spectrum are favored by the data, whereas GLEs with small to moderate memory spectra are insufficient.

## 1. INTRODUCTION

Over the last two decades, advances in microscopy have provided scientists with unprecedented access to observing the fluctuating dynamics of microparticles in biological fluids. An important and ubiquitous observation from these experiments is that microparticle diffusion in biological fluids is often not well-described by simple Brownian motion. The most prominent gauge for the departure from the Brownian regime is the mean-squared displacement (MSD) of a particle’s trajectory  $X(t)$ :

$$\langle X^2(t) \rangle = \mathbb{E} [(X(t) - X(0))^2], \quad t \geq 0.$$

While the MSD of classical viscous diffusion scales linearly with time,  $\langle X^2(t) \rangle \propto t$ , there are now numerous biological examples of sublinear MSD growth:

$$(1) \quad \langle X^2(t) \rangle \propto t^\alpha$$

for some  $\alpha \in (0, 1)$  and  $t$  ranging over some experimental time frame. This MSD scaling behavior is known as *anomalous subdiffusion*. Examples of this behavior include Adeno-associated virus in cytoplasm (Seisenberger et al., 2001), lipid granules in living fibroblasts (Caspi and Granek, 2000) and living yeast cells (Tolić-Nørrelykke et al., 2004; Selhuber-Unkel et al., 2009; Jeon et al., 2011),

<sup>\*</sup>University of Waterloo, <sup>†</sup>Harvard University, <sup>‡</sup>University of North Carolina at Chapel Hill, <sup>§</sup>University of South Carolina, <sup>¶</sup>University of Florida.

tracer particles in F-actin networks (Wong et al., 2004a), RNA in *E. coli* (Golding and Cox, 2006), telomeres in the nucleus of mammalian cells (Bronstein et al., 2009), tracers in a Dextran solution intended to mimic diffusion in a crowded environment (Ernst et al., 2012), and passive micron diameter beads in human bronchial epithelial cell culture mucus (Hill et al., 2014).

Anomalous subdiffusion can potentially be caused by several physical mechanisms: it might reflect the viscoelastic memory spectrum of a complex fluid medium (Mason and Weitz, 1995); it might be evidence of hindered motion in a crowded environment (Ernst et al., 2012); it could arise from long-term trapping events that occur due to binding with a physically constrained substrate in the fluid (Saxton, 2007); or it could result from caging events that occur due to particle movement within and between pores in an immersed mesh structure (Wong et al., 2004a). It follows that rigorous stochastic modeling and statistical inference can have a direct impact not only on investigations into the basic science of microparticle movement, but also on the applications of this science to diagnosis of disease (Georgiades et al., 2014), disease progression (Hill et al., 2014) and the engineering of drug delivery (Lai et al., 2007; Cone, 2009; Ensign et al., 2012).

Mucus is a particularly important and challenging biological fluid to understand. Thin mucosal layers line the eyes, nasal cavity, lungs, gut and female reproductive tract, and stand as the body's first line of defense against foreign microscopic toxins, particulates and pathogens. However, our understanding of how these foreign bodies interact with and move through mucus remains incomplete. The microstructure of human lung mucus, our motivating biological fluid, is strikingly complex. By weight, mucus is mostly water, (92–98 wt%). The remaining portion consists of diverse small molecules including proteins, immunoglobulins, salts, and dead cells, along with a variety of larger polymeric molecular species (the primary ones are in the mucin molecule family) that have only recently have been identified (Carlstedt et al., 1982, 1983a,b; Carlstedt and Sheehan, 1984; Thornton and Sheehan, 2004). These species assemble to create a heterogeneous 3D mesh with repulsive or attractive interactions specific to the molecular microstructure and surface chemistry of the observed particle. The theoretical challenge of predicting the behavior of embedded microparticles from this unknown biological molecular complexity is daunting and not likely to be overcome soon.

Nevertheless, strong signals in particle tracking data are repeatedly observed. At the coarsest descriptive scale, mucus can be thought of as a viscous fluid (salt water) that contains a suspended and entangled network of semi-flexible mucin fibers. Because mucus is comprised of a complex mixture of molecules having a wide range of sizes and chemical interactions, the effective mesh size of the mucin network varies both within and across samples. Microparticles moving in mucus therefore exhibit very different stochastic path properties depending on their size (effective hydrodynamic radius) (Wong et al., 2004b), repulsive versus attractive interactions with the mucus microstructure (Suk et al., 2009), and the weight percentage (wt%) of solids suspended in the fluid (Hill et al., 2014). For example, small entities like antibodies (5 nm effective

radius) and virions (up to 60 nm) have little interaction with the mucin network and have behavior that is well-described by simple Brownian motion (Saltzman et al., 1994; Olmsted et al., 2001). On the other hand, amine-modified and carboxylated particles ranging from 200 nm to 1  $\mu\text{m}$  in radius have been shown to exhibit subdiffusive behavior (Dawson et al., 2003; Suk et al., 2007; Lai et al., 2007). Interestingly, unlike the well-established relationship between particle radius and its diffusivity in a *viscous* fluid (the leading coefficient of the particle’s linear MSD), there is no theoretically or experimentally established scaling between particle radius and the exponent of an associated sublinear MSD in a *viscoelastic* fluid.

**1.1. The Problem.** While a sublinear MSD is a clear indicator of non-Brownian movement, MSD is a summary statistic that does not preserve other important information contained in the observed time series. There is an important distinction between using a summary statistic for parameter estimation – within the framework of fitting a single stochastic model – and using the same statistic to distinguish between two or more models. Unfortunately, many efforts in the recent particle tracking literature ignore this subtlety. Models are chosen to mimic certain aspects of popular summary statistics, but these choices do not stand up under an analysis that does not compress the data before model selection.

To be specific, the majority of inferential methods to date rely heavily on a path-by-path empirical estimate of the MSD, calculated from discrete observations  $\{X_0, \dots, X_N\}$  of  $\{X(t)\}_{t \in [0, T]}$  at equal time intervals of length  $\Delta t = T/N$ . This so-called *pathwise MSD* is defined by (e.g., Didier et al., 2012)

$$(2) \quad \langle \widehat{X^2(t)} \rangle = \frac{1}{N-h+1} \sum_{n=0}^{N-h} (X_{n+h} - X_n)^2, \quad t = h \cdot \Delta t.$$

The appeal of this “within-sample” statistic is that, without access to a large number of sample paths, the estimate of the ensemble MSD across samples can be very noisy. Assuming the underlying stochastic process is in some sense ergodic, averaging over numerous particles’ pathwise MSDs provides a more accurate estimate of  $\langle X^2(t) \rangle$ . However, biological fluids are often heterogeneous, and a major scientific challenge is to look at particle paths in different spatial locations within the same fluid to assess this heterogeneity (Valentine et al., 2001). In this case, averaging over several distinct paths to estimate  $\langle X^2(t) \rangle$  results in a significant loss of information. Moreover, even in a homogeneous medium, neither the pathwise MSD nor its theoretical counterpart suffice to fully characterize the stochastic particle displacement process  $X(t)$ . While either of these might be sufficient *within* a (parametric) family of statistical models, they are not sufficient *across* models, which often leads to invalid model selection procedures if one fails to account for ancillary information (Robert et al., 2011).

To illustrate this point, consider the following fundamental issue in the field. Due to laboratory constraints, the duration of particle traces are typically limited to seconds or minutes, but most biological processes of interest take place over hours or days. A primary scientific objective is to extrapolate quantitative predictions for properties like first-passage times of foreign

particles through protective mucosal layers – a process that is important both to investigators who want to develop new vaccination strategies (Whaley et al., 2010) as well to those who are engineering new drug delivery techniques (Lai et al., 2009; Ensign et al., 2012). For these purposes, the MSD statistic is woefully inadequate. This is demonstrated by contrasting two stochastic models that have been popularly employed by particle tracking investigators: Fractional Brownian Motion (fBM) (Mandelbrot and Van Ness, 1968) and the Continuous-Time Random Walk (CTRW) (Metzler and Klafter, 2000). Both of these processes can be parameterized so that  $\langle X^2(t) \rangle = Ct^\alpha$  for a given pair of constants  $C > 0$  and  $\alpha \in (0, 1)$ . However, the mean time for fBM to escape from a bounded interval is *finite* (O’Malley et al., 2011), while for subdiffusive CTRW it is *infinite* (Rangarajan and Ding, 2000). In other words, the escape time contains ancillary information about these models which is not contained in the MSD. A more extreme example by Meroz et al. (2011) has recently demonstrated that matching the stationary distribution of a statistical ensemble is also insufficient for prediction of first-passage times.

**1.2. Our Contribution.** Microparticle displacement data continue to proliferate and statistical methods of selecting between different candidate models remains an active area of research. Our principal aim in this article is to perform a rigorous, likelihood-based model comparison procedure to distinguish among two key anomalous subdiffusion models. Our secondary aim is to assess which features of the data these models do capture and which ones they do not through. To this end, we analyze data describing the motion of 500 nm radius polystyrene “tracer” particles in 2.5 wt% mucus (Hill et al., 2014). We picked this collection of paths because they exemplify the essential problem in the field of particle heterogeneity. This is illustrated in Figure 1. In our data set (further described in Section 3.1), the physical environment is homogeneous in the sense that we have controlled for a qualitatively similar fluid environment for essentially identical particles. However, the distribution of pathwise MSD estimates (center panel of Figure 1) is considerably more widely spread than one would expect from an independent and identically distributed (iid) sample from a uniform population.

This spread in pathwise MSD curves has been widely observed for particles in biological fluids and is often referred to as the *ergodicity breaking* property (Lubelski et al., 2008). In addition to capturing subdiffusive behavior, the CTRW model exhibits ergodicity breaking among iid particle trajectories, whereas the fBM model does not. This is often cited as a major argument in support of the CTRW for modeling viscoelastic diffusion (Lubelski et al., 2008; Metzler et al., 2009; Jeon and Metzler, 2010; Jeon et al., 2011; Burov et al., 2011; Meroz et al., 2013). However, the CTRW model has also been the subject of numerous criticisms. For one, it produces a stochastic process with discontinuous paths. More importantly, Szymanski and Weiss (2009) have noted that subdiffusion induced by crowding can not be explained by CTRW. They observed that the particle paths in their data set were Gaussian and appeared to have stationary increments – both properties which are not exhibited by subdiffusive CTRW. On the other hand, both of these are key properties of fBM. Parallel to the work of Szymanski and Weiss, Magdziarz et al. (2009)

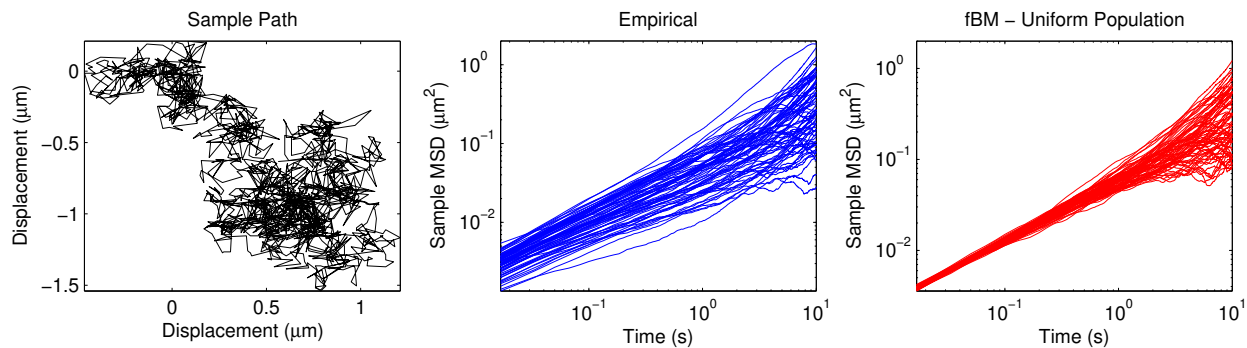


FIGURE 1. Left to right: (a) Representative sample path of a 500 nm radius tracer bead in 2.5 wt% mucus. (b) Ensemble of pathwise MSD curves for 76 tracer bead paths under essentially identical experimental conditions. (c) Pathwise MSDs for 76 simulated tracer particle paths from the best-fitting fBM model to the experimental data in (a).

and [Magdziarz and Klafter \(2010\)](#) used the property that fBM has finite  $p$ -th variation to analyze nanoparticle motion in live *E. coli* cells ([Golding and Cox, 2006](#)). In this same spirit, [Tejedor et al. \(2010\)](#) proposed a method of positively identifying fBM by an analysis of mean maximal excursions. More recently, [Ernst et al. \(2012\)](#) used a fractal property called asphericity to argue that diffusion in a crowded dextran solution is better described by fBM than by CTRW. Finally, in [Hill et al. \(2014\)](#), the shape of the autocorrelation function (ACF) of increments of bead paths in human lung mucus was used to argue for fBM over CTRW.

Therefore, in this article we will not focus on an fBM versus CTRW dichotomy. Rather, we will compare two Gaussian processes with stationary increments that can both be tuned to mimic subdiffusive MSD scaling over the experimental time range. These two candidate models are fBM, and a Generalized Langevin Equation (GLE) detailed in Section 2. While the former is a well-known stochastic process with interesting behavior both at short and long time scales, a key feature of the latter is that it can be developed in terms of fundamental physical laws governing the interactions between particles in viscoelastic equilibrium systems. As parametric models, both fBM and the GLE completely determine the likelihood function for the observed data. Fitting these models is discussed in Section 3, including a detailed analysis of the measurement error – in the absence of which a cursory treatment of the noise would have almost entirely masked the actual signal.

In Section 4, we harness the full power of the observed data likelihood for model comparison by the computation of Bayes factors. A common criticism of this approach relies on the choice of prior parameter distribution, which can influence considerably the preference for one model over the other. To address this issue, we utilize a data-driven prior obtained by hierarchical modeling over a collection of sample paths. Indeed, the hierarchical model can naturally account for particle heterogeneity and ergodicity breaking. We present an efficient method for approximately fitting the hierarchical model, of general interest and applicable in a broader setting.

Finally, in Section 5 we assess the goodness-of-fit of the candidate models through a variety of posterior predictive checks. While highly sensitive residual tests provide significant evidence against the Gaussian assumption, the models do seem to capture the second-order properties of the data, both on short- and long-range time scales. An interpretation of these results and discussion of further work is presented in Section 6.

## 2. OVERVIEW OF CANDIDATE MODELS

Both Fractional Brownian Motion (fBM) and the Generalized Langevin Equation (GLE) are stochastic continuous-time models which have been independently posited and applied to the analysis of subdiffusive behavior. Both models feature stationary Gaussian increments and continuous sample paths, with some additional properties given below.

**2.1. Fractional Brownian Motion.** A simple extension to Brownian motion for modeling subdiffusion in the bead displacement  $X(t)$  can be obtained by allowing its increments to be correlated. This model considers  $X(t)$  to be a fractional Brownian motion with drift:

$$(3) \quad X(t) = \mu t + \sigma B_H(t).$$

Here,  $B_H(t)$  is driftless fBM, a zero-mean Gaussian process with  $B_H(0) = 0$  and covariance

$$\text{cov}(B_H(t), B_H(s)) = \frac{1}{2} \left( |t|^{2H} + |s|^{2H} - |t-s|^{2H} \right), \quad 0 < H < 1.$$

For  $\mu = 0$ , we have  $\langle X^2(t) \rangle = \sigma^2 t^{2H}$  such that the MSD scaling exponent in (1) is given by  $\alpha = 2H$ . The Hurst parameter  $H$  is used to describe fBM's long-range effects. That is, let  $x_n = X(n\Delta t + \Delta t) - X(n\Delta t)$  be particle trajectory increments of length  $\Delta t$ . Then

$$(4) \quad \text{cov}(x_n, x_{n+k}) = \frac{1}{2} \sigma^2 (\Delta t)^{2H} \left( |k+1|^{2H} + |k-1|^{2H} - 2|k|^{2H} \right).$$

While the  $x_n$  are not independent, (4) shows that they are stationary. For  $H = 1/2$ , the fBM model (3) reduces to ordinary Brownian motion with drift  $\mu$ . For  $H \neq 1/2$ , fBM has long-range memory effects, in the sense that the autocorrelation (4) has power law decay. It is worth noting that (driftless) fBM is the unique stochastic process having (i) continuous paths, (ii) stationary (but dependent) increments, and (iii) possessing the self-similarity property:  $B_H(at) \stackrel{D}{=} |a|^H B_H(t)$ .

**2.2. A Generalized Langevin Equation for Viscoelastic Subdiffusion.** While fBM is one of many statistical models featuring subdiffusive behavior, it also has a rigorous physical interpretation as the limit of an interacting particle system in thermal equilibrium (Kubo, 1966; Zwanzig, 2001; Kou, 2008). This physical interpretation (about to be described) serves as the basis for a second candidate model for subdiffusive tracer particles in a viscoelastic medium.

A fundamental model of diffusion derived from Newtonian physics is the so-called *Langevin Equation*, which describes the velocity of a particle in a viscous fluid by setting up a force-balance equation satisfying Newton's second law:

$$m\dot{X}(t) = F_{\text{drag}}(t) + F_{\text{thermal}}(t).$$

Here,  $\ddot{X}(t)$  is the acceleration of the particle and  $m$  is its mass. The driving thermal force  $F_{\text{thermal}}(t)$  and the resistive “drag” force  $F_{\text{drag}}(t)$  both originate from the same source – collisions between the multitude of particles in the fluid medium and the tracer particle of interest – and precisely offset each other in an equilibrium system. In the Langevin model,  $F_{\text{thermal}}(t)$  is assumed to be white noise. Written as a stochastic differential equation in the velocity of the particle  $V(t) = \dot{X}(t)$ , the Langevin equation is

$$(5) \quad m dV(t) = -\gamma V(t) dt + \sqrt{2k_B T \gamma} dB(t),$$

where  $\gamma$  is the viscous drag constant,  $k_B$  is Boltzmann’s constant,  $T$  is the temperature of the system, and  $B(t)$  is Brownian motion. The specific relation between the coefficients of  $V(t)$  and  $B(t)$  on the right hand side of (5) is necessary for it to define a physically valid process. This precise balance between drag and thermal forces is known as the Fluctuation-Dissipation theorem in statistical mechanics (Kubo, 1966; Zwanzig, 2001).

The integrated process  $X(t) = \int_0^t V(s) ds$  is sometimes referred to as “physical Brownian motion.” Indeed, the autocorrelation of the stationary solution to (5) is given by  $\mathbb{E}[V(t)V(s)] = \frac{k_B T}{m} e^{-\gamma|t-s|/m}$ . As  $m \rightarrow 0$ , this converges to a Dirac  $\delta$ -function, implying that physical Brownian motion converges to mathematical Brownian motion  $B(t)$  in the zero-mass limit. Just as mathematical Brownian motion is an idealization of a physically motivated model (the integrated Langevin equation) one can think of fractional Brownian motion as a mathematical idealization of a so-called *Generalized Langevin Equation* (GLE).

A key hypothesis in the theoretical development of the Langevin equation is the assumption that there is separation of time scales between the dynamics of the focal particle of interest and the dynamics of the smaller particles in the surrounding medium (Kubo, 1966; Zwanzig and Bixon, 1970; Hauge and Martin-Löf, 1973; Kupferman, 2004; Kou and Xie, 2004). When there is no such separation of time scales, the thermal force has a memory effect which is generally modeled by taking  $F(t) = F_{\text{thermal}}(t)$  to be a mean-zero stationary Gaussian process with covariance

$$\text{cov}(F(t), F(s)) = \gamma(|t - s|).$$

A Generalized Langevin Equation is then obtained by invoking the Fluctuation-Dissipation theorem to precisely balance  $F_{\text{drag}}(t)$  with  $F_{\text{thermal}}(t)$ :

$$(6) \quad m\dot{V}(t) = - \int_{-\infty}^t \gamma(t-s)V(s) ds + \sqrt{k_B T} F(t).$$

A formal derivation of (6) can be obtained from first principles using Hamiltonian dynamics in a heat bath of harmonic oscillators (Zwanzig, 2001; Kou, 2008; Ottobre and Pavliotis, 2011).

Depending on the form of the memory kernel, the GLE can exhibit either transient or asymptotic (as  $t \rightarrow \infty$ ) anomalous subdiffusion (Morgado et al., 2002; Kou and Xie, 2004; Kneller, 2011). In fact, subdiffusive fBM can be obtained *exactly* in the zero-mass limit of a particular GLE (Kou, 2008, Theorem 2.2). The thermal force required is  $F(t) = \dot{B}_H(t)$ , the so-called *fractional Gaussian*

Noise process defined for  $1/2 \leq H < 1$ . In this case, the displacement process  $X(t) = B_{H^*}(t)$  is fBM with Hurst parameter  $H^* = 1 - H$ , such that  $0 < H^* \leq 1/2$ .

The use of the GLE for dynamical modeling in viscoelastic fluids was brought to prominence in the seminal work of [Mason and Weitz \(1995\)](#). The authors proposed a generalized Stokes-Einstein relationship ([Squires and Mason, 2010](#)) that relates material properties of a viscoelastic fluid (the storage and loss moduli) to the memory kernel of embedded particles. The fundamental hypothesis of the field, which is called *passive microrheology*, is that a sufficient description of particle trace properties can yield information about the surrounding medium.

It is a common assumption in linear viscoelastic theory (e.g., [Soussou et al., 1970](#); [Ferry, 1980](#); [Park and Schapery, 1999](#); [Ghoreishy, 2012](#)) that the fluid system has a finite number of distinct relaxation times  $\tau_1, \dots, \tau_K$  which are used to parametrize a sum-of-exponentials form of memory kernel called a *Prony series*:

$$(7) \quad \gamma_K(t) = \sum_{k=1}^K c_k \exp(-|t|/\tau_k).$$

Several authors have proposed to model memory in the microparticle GLE by such a Prony series (e.g., [Schaink et al., 2000](#); [Fricks et al., 2009](#); [Indei et al., 2012](#)). The thermal force  $F(t)$  can then be written as a sum of independent Ornstein-Uhlenbeck processes with corresponding decorrelation times. Such a formulation allows for a Markovian SDE representation of the GLE and, in principle, makes maximum likelihood estimation of the coefficients and relaxation times possible. However, when the number of modes  $K$  is even moderately large, the Prony series GLE model becomes overparametrized and has a considerable lack of model identifiability for the typical amount of data that is experimentally available ([Fricks et al., 2009](#)). To compensate, authors have therefore chosen to impose a structure on the so-called ‘‘relaxation spectrum’’  $\{\tau_k\}_{k=1}^K$ . The elements of this spectrum may be drawn from some random distribution ([Kupferman, 2004](#)), might arise from some network connectivity structure ([McKinley, 2009](#)), or be inspired by spectra associated with the Rouse and Zimm models in polymer physics ([Rouse, 1953](#); [Rubinstein and Colby, 2003](#); [McKinley et al., 2009](#)).

In this paper, we follow [McKinley et al. \(2009\)](#) and adopt the Generalized Rouse spectrum:

$$(8) \quad \tau_k = \tau_1(K/k)^\rho, \quad c_k = \eta/K.$$

The parameters of the model are:  $K$ , the number of modes;  $\tau_1$ , the smallest relaxation time;  $\eta$ , a scale factor; and  $\rho$ , a shape parameter that can be used to capture subdiffusive behavior. Indeed, we show in the Supplementary Material (S1) that for the Prony series kernel,  $\gamma_K^{\text{Rouse}}(t) \sim t^{-1/\rho}$  as  $K \rightarrow \infty$  for large  $t$ , such that for a large number of modes we have asymptotic subdiffusion,  $\langle X^2(t) \rangle \sim t^\alpha$  with  $\alpha = 1/\rho$  in the zero-mass limit. Thus, our viscoelastic GLE model is given by

$$(9) \quad \int_{-\infty}^t \gamma_K^{\text{Rouse}}(t-s)V(s) ds dt = \sqrt{k_B T} F(t),$$

which corresponds to (6) with  $m \rightarrow 0$ . The displacement process  $X(t) = \int_0^t V(s) ds$  is also a continuous stochastic process with stationary increments,  $x_n = X(n\Delta t + \Delta t) - X(n\Delta t)$ . These increments are Gaussian with mean  $\mathbb{E}[x_n] = 0$  and autocorrelation

$$(10) \quad \text{cov}(x_n, x_{n+k}) = \sigma^2 \left( C_0^2 \Delta t \delta(k) + \sum_{j=1}^{K-1} \frac{C_j^2}{2r_j} \left( 2e^{-r_j|k|} - e^{-r_j|k-1|} - e^{-r_j|k+1|} \right) \right),$$

where  $\sigma^2 = 2k_B T / \eta$ ,  $\delta(k)$  is the Dirac  $\delta$ -function, and expressions for  $C_j$  and  $r_j$  are provided in S3.

### 3. DATA COLLECTION AND MODEL FITTING

**3.1. Data Collection.** Our data collection methods are fully detailed in Hill et al. (2014). To summarize, mucus was harvested from primary human bronchial epithelial (HBE) cell cultures. We placed 1  $\mu\text{m}$  polystyrene particles with carboxyl surface chemistry in 1 cm discs containing 5  $\mu\text{L}$  of mucus. The bead surface treatment was chosen to minimize binding affinities between the beads and mucins in the fluid environment. In this way, we argue that the viscoelasticity of the fluid medium is the primary contributing factor to non-Brownian aspects of particle trace statistics. The motion of the beads was recorded at 60 frames per second and bead position was determined by Video Spot Tracker (<http://cisimm.cs.unc.edu/downloads/>).

Experimental particle trajectories were obtained for various levels of mucus concentration, ranging from 1 wt% to 5 wt%. Motion in 1 wt% was very similar to Brownian motion, while particles paths in 5 wt% mucus exhibited a wide range of behaviors. The most uniform group showing persistent non-Brownian behavior was for 2.5 wt% and so we used this group for the analysis which follows.

While the particle trajectories were recorded in a two-dimensional plane (Figure 1), we have restricted ourselves to a one-dimensional analysis which greatly simplifies modeling and related calculations. A total of 76 trajectories at 2.5 wt% were recorded, of which 10 representative displacement curves are displayed in Figure 2. The data were recorded at  $\Delta t = 1/60$  frames per second for 30 seconds each ( $N = 1799$  observations).

**3.2. Model Fitting.** Denote the  $N = 1799$  observations of a given particle's trajectory by  $X = (X_0, \dots, X_N)$ ,  $X_n = X(n\Delta t)$ . Both the fBM and GLE models are nonstationary but have stationary increments. That is,  $\mathbf{x} = (x_1, \dots, x_N)$  with  $x_n = X_n - X_{n-1}$  is a stationary process. For the fBM model (3),  $\mathbf{x}$  is multivariate Gaussian with mean  $\mathbb{E}[x_n] = \mu\Delta t$  and autocorrelation given in (4). The log-likelihood function is

$$\ell(\mu, \sigma, H | \mathbf{x}) = -\frac{1}{2} \left\{ \frac{(\mathbf{x} - \mu\Delta t)' \mathbf{V}_H^{-1} (\mathbf{x} - \mu\Delta t)}{\sigma^2} + N \log(\sigma^2) + \log(|V_H|) \right\},$$

where  $\mathbf{V}_H$  is a symmetric Toeplitz matrix with  $[\mathbf{V}_H]_{ij} = \text{cov}(x_i, x_j) / \sigma^2$ . Since  $\mathbf{V}_H$  is a Toeplitz matrix, it can be inverted using the Durbin-Levinson algorithm in  $O(N^2)$  operations. This is in contrast to general matrix inversion which is  $O(N^3)$ . For this reason, it is computationally more efficient to work with the stationary increments.

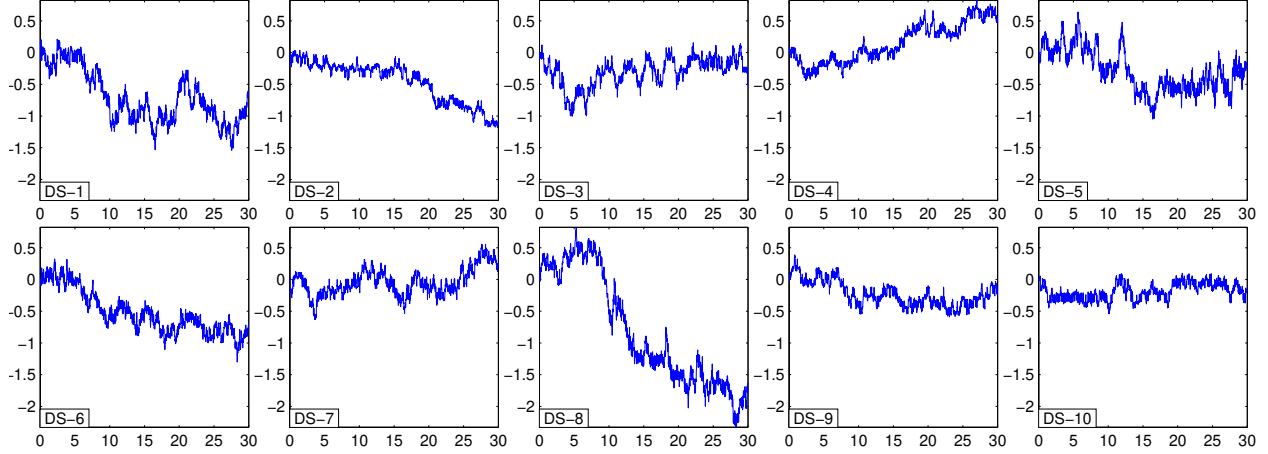


FIGURE 2. Displacements curves  $X(t)$  for 10 representative bead trajectories with 2.5 wt% mucus concentration. The  $x$ -axis for these curves is time (s) and the  $y$ -axis is displacement ( $\mu\text{m}$ ). The data have been centered such that  $X(0) = 0$ .

To estimate the parameters of the fBM model (3) in a Bayesian setting, we employ the family of conjugate priors:

$$(11) \quad \begin{aligned} H &\sim \pi(H), \\ \sigma^2 | H &\sim \text{Inv-Gamma}(\alpha_H, \beta_H), \\ \mu | \sigma, H &\sim \mathcal{N}(\lambda_H, \sigma^2 / \Omega_H) \end{aligned}$$

where  $\alpha_H$ ,  $\beta_H$ ,  $\lambda_H$ , and  $\Omega_H$  can each depend on the value of  $H$ . For this choice of prior, the posterior distribution is

$$(12) \quad \begin{aligned} H | \mathbf{x} &\sim \pi(H) \times \frac{\Lambda(\alpha_H, \beta_H)}{\Lambda(\alpha_H + N/2, \beta_H + \hat{\beta}_H)} \left( \frac{\Omega_H}{(T_H + \Omega_H) |V_H|} \right)^{1/2}, \\ \sigma^2 | H, \mathbf{x} &\sim \text{Inv-Gamma}(\alpha_H + N/2, \beta_H + \hat{\beta}_H), \\ \mu | \sigma, H, \mathbf{x} &\sim \mathcal{N}(\hat{\lambda}_H, \sigma^2 (T_H + \Omega_H)^{-1}) \end{aligned}$$

where expressions for  $\Lambda(\cdot, \cdot)$ ,  $\hat{\beta}_H$ ,  $T_H$ , and  $\hat{\lambda}_H$  are provided in S2.

Marginal posteriors of the memory parameter  $p(H | \mathbf{x})$  for the 76 tracer bead trajectories are displayed in Figure 3. These posteriors are obtained from the noninformative prior

$$(13) \quad \pi(\mu, \sigma, H) \propto 1/\sigma$$

which is also a member of the conjugate family (11). All credible 95% intervals are well below  $H = 1/2$ , indicating a clear departure from Brownian motion and its underlying assumption of ordinary diffusion.

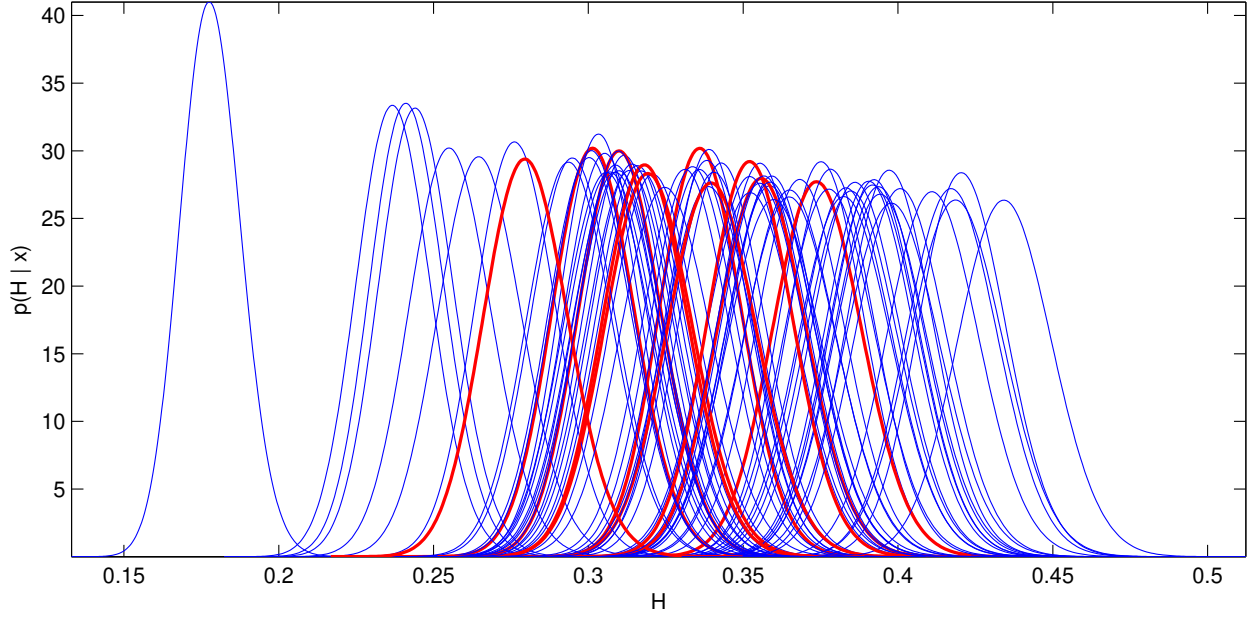


FIGURE 3. Posterior distributions  $p(H | \mathbf{x})$  for 76 tracer bead displacement curves using the prior  $\pi(\mu, \sigma, H) \propto 1/\sigma$ . The posteriors for the 10 datasets from Figure 2 are highlighted in red.

For the viscoelastic GLE model (9) with generalized Rouse spectrum, the log-likelihood function has a similar form:

$$\ell(\rho, \tau_1, \sigma | \mathbf{x}) = -\frac{1}{2} \left\{ \frac{\mathbf{x}' [\mathbf{V}_K(\rho, \tau_1)]^{-1} \mathbf{x}}{\sigma^2} + N \log(\sigma^2) + \log(|\mathbf{V}_K(\rho, \tau_1)|) \right\}.$$

The parameters of this model are  $\rho$ ,  $\tau_1$ , and  $\sigma$ , with the number of relaxation times being fixed at  $K = 4$  and  $K = 200$  modes. The choice of  $K = 4$  is intended to represent those who have used a low number of modes to model viscoelastic diffusion (e.g., Schaink et al., 2000; Fricks et al., 2009; Indei et al., 2012; Córdoba et al., 2012; Baczewski and Bond, 2013), while the choice of  $K = 200$  serves to approximate the limit  $K \rightarrow \infty$  which induces asymptotically subdiffusive behavior.

For the GLE model (9), a conjugate prior of the form

$$(14) \quad \begin{aligned} \rho, \tau_1 &\sim \pi(\rho, \tau_1), \\ \sigma^2 | \rho, \tau_1 &\sim \text{Inv-Gamma} \left\{ \alpha(\rho, \tau_1), \beta(\rho, \tau_1) \right\} \end{aligned}$$

leads to an analytical expression for the joint posterior  $p(\rho, \tau_1 | \mathbf{x})$ . The specific form of prior we adopted here was

$$(15) \quad \begin{aligned} \pi(\rho) &\propto 1, \\ \log(\tau_1) | \rho &\sim \mathcal{N}(-6.91, 2.68^2), \\ \pi(\sigma | \rho, \tau_1) &\propto 1/\sigma. \end{aligned}$$

This corresponds to default noninformative priors for  $\rho$  and  $\sigma$ , and a proper log-Normal prior for the minimal relaxation time  $\tau_1$ . We retained a proper prior for  $\tau_1$  after examining a host of improper priors (e.g., Lebesgue,  $\pi(\tau_1) \propto 1/\tau_1$ ) which all resulted in improper posteriors. Moreover, the 76 datasets displayed considerable heterogeneity in the magnitude of  $\tau_1$  which is conveniently measured on the log-scale. The numerical values for the prior mean and standard deviation of  $\nu = \log(\tau_1)$  were chosen for  $\tau_1$  to have 99% probability a priori of falling between  $1 \mu\text{s}$  and  $1 \text{s}$ .

Posterior distributions of  $\rho$  and  $\nu = \log(\tau_1)$  for the 76 datasets are displayed in Figure 4 using both  $K = 4$  and  $K = 200$  modes. Here we have imposed the restriction  $\rho > 0$ , with

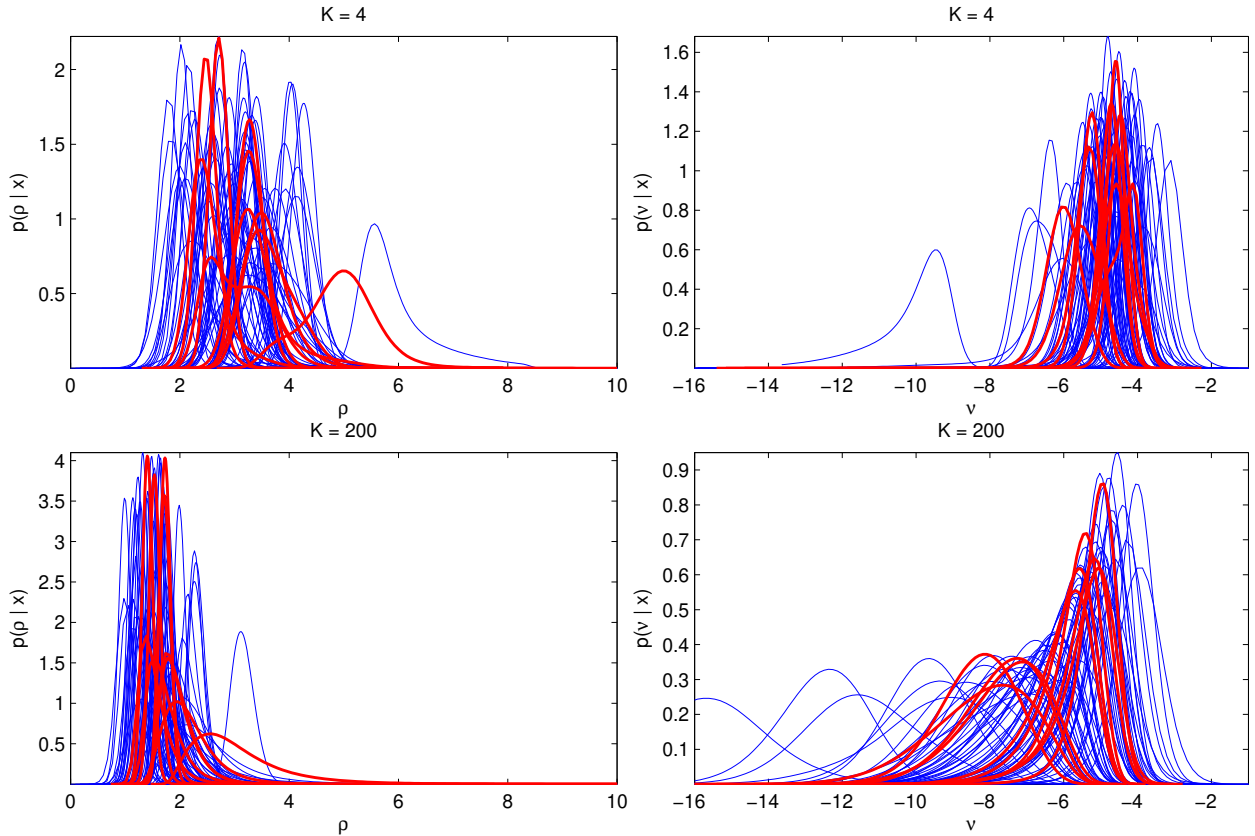


FIGURE 4. Posterior distributions of  $\rho$  and  $\nu = \log(\tau_1)$  for 76 tracer bead displacement curves.

subdiffusion occurring only for  $\rho > 1$ . The region  $0 < \rho < 1$  corresponds to *superdiffusive* behavior,  $\langle X^2(t) \rangle \sim t^\alpha$  with  $\alpha > 1$ . While some of the 95% credible intervals in Figure 4 do contain  $\rho = 1$ , the posterior analysis predominantly favors subdiffusive behavior  $\rho > 1$ .

Figure 5 displays the induced values of the subdiffusion coefficient  $\alpha$  for both the fBM model and the GLE model with  $K = 200$  relaxation times (hereafter, GLE-200). The induced values of  $\alpha$  for these models are  $\alpha = 2H$  and  $\alpha = 1/\rho$  respectively. The posterior means are close to the diagonal line, indicating that inference for the subdiffusion coefficient is quite similar for both

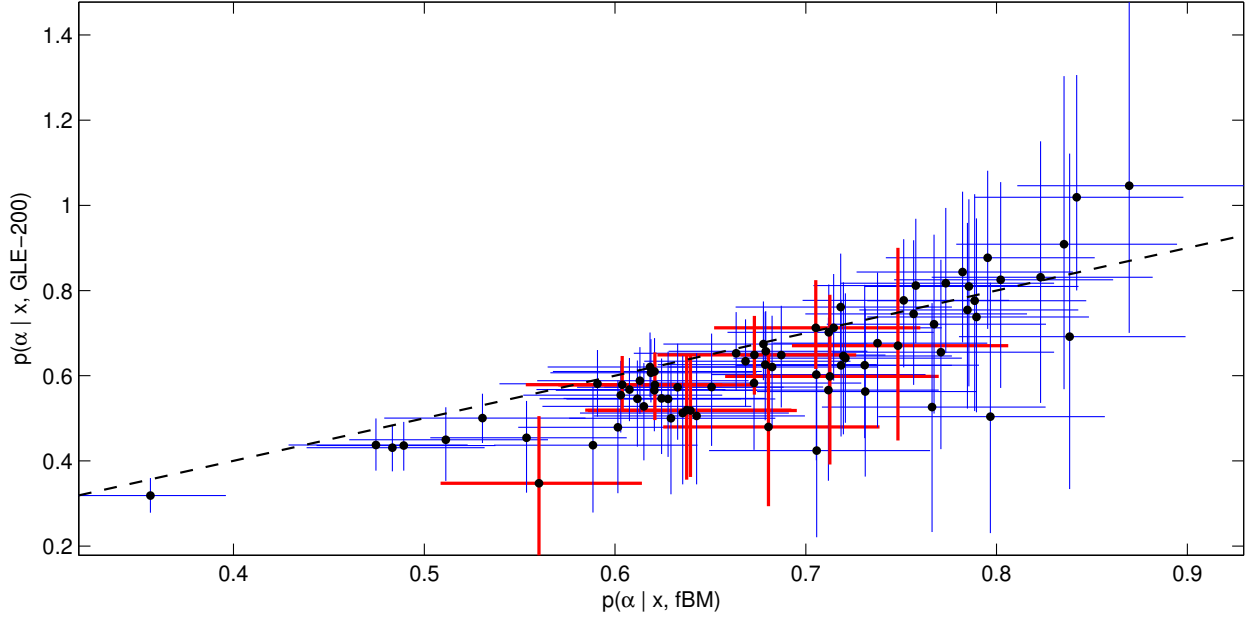


FIGURE 5. Posterior distributions of the subdiffusion coefficient  $\alpha$  (mean and 95% credible intervals) for the fBM and GLE-200 models. Values on the dashed line indicate identical posterior inference for  $\alpha$  with both models.

models, with GLE-200 typically giving lower values except in the vicinity of superdiffusion,  $\alpha > 1$ .

**3.3. Measurement Error.** We briefly discuss the effect of measurement error on our analysis. All observations of tracer bead displacement are corrupted by a “detection error” due to mechanical vibrations of the recording device. A naive model for the measurement error is that the observed data  $\mathbf{y} = (y_1, \dots, y_N)$  are

$$(16) \quad y_n = x_n + \epsilon_n, \quad \epsilon_n \stackrel{\text{iid}}{\sim} \mathcal{N}(0, \nu^2),$$

where  $x_n$  are increments of the true particle displacement and the measurement error  $\epsilon = (\epsilon_1, \dots, \epsilon_N)$  are independent of  $X(t)$ . However, uncertainty in the error magnitude  $\nu$  can have a considerable impact on inferential results, as illustrated in S4.

Fortunately, the experimental setup allowed for the measurement error to be quantified separately. That is, the tracer bead particles were allowed to dry onto their glass mountings, immobilizing them completely (no displacement). Thus, the observed displacement of these beads was purely due to mechanical vibrations in the recording device. The analysis in S4 indicates that the measurement error is several orders of magnitude smaller than the observed signal. Indeed, several simulations suggest that the measurement error in our experiments have a negligible effect on inferential results. We proceed with our analysis under the assumption that the measurement error on our observed particle trajectories is effectively zero.

#### 4. BAYESIAN MODEL COMPARISONS

In the Bayesian framework we have adopted, a natural quantitative approach to model selection is through the use of Bayes factors (Jeffreys, 1961; Kass and Raftery, 1995; Green, 1995). Bayes factors have been widely used to compare complex and non-nested models of biological systems (Lartillot and Philippe, 2006; Vyshemirsky and Girolami, 2008; Toni et al., 2009; Li and Drummond, 2012), and recently, to analyze MSD curves of particle motion in live cells (Monnier et al., 2012). However, the strategy adopted by Monnier et al. consists of least-squares fitting to empirical MSD curves. As these are subject to considerable sampling variation, a great deal of selection power is lost by renouncing a fully parametric likelihood-based approach. Furthermore, the approach relies solely on summary statistics (the pathwise MSD and its variants), in which case a great deal of care must be employed to insure that Bayesian model selection leads to statistically valid results (as discussed in Section 1.1).

Suppose that we wish to compare two models  $M_1$  and  $M_2$  which assign distributions  $p(\mathbf{x} | \boldsymbol{\theta}_i, M_i)$  to the observed data  $\mathbf{x}$ , where  $\boldsymbol{\theta}_i$  denotes the parameter vector corresponding to model  $M_i$ . Then for proper priors  $\pi(\boldsymbol{\theta}_i | M_i)$  on the parameters of each model, the posterior distribution of model  $M_i$  is

$$(17) \quad p(M_i | \mathbf{x}) = \frac{\pi(M_i) f_i(\mathbf{x})}{\pi(M_1) f_1(\mathbf{x}) + \pi(M_2) f_2(\mathbf{x})},$$

where

$$f_i(\mathbf{x}) = \int p(\mathbf{x} | \boldsymbol{\theta}_i, M_i) \pi(\boldsymbol{\theta}_i | M_i) d\boldsymbol{\theta}_i$$

is the marginal data distribution for model  $M_i$ . The Bayes factor is defined as a ratio of posterior to prior model odds,

$$\text{BF} = \frac{p(M_1 | \mathbf{x}) / p(M_2 | \mathbf{x})}{\pi(M_1) / \pi(M_2)} = \frac{f_1(\mathbf{x})}{f_2(\mathbf{x})},$$

which can be used to assess the relative plausibility of  $M_1$  to  $M_2$ . An attractive feature of this measure is that it does not depend on the prior probability  $\pi(M_i)$ . Equivalently, the Bayes factor is simply the posterior odds  $p(M_1 | \mathbf{x}) / p(M_2 | \mathbf{x})$  when a lack of preference between either model is expressed as equal prior probabilities  $p(M_1) = p(M_2) = 1/2$ . In this case we have the monotone transformation  $p(M_1 | \mathbf{x}) = \text{BF} / (1 + \text{BF})$ , which we have used here to interpret the Bayes factor calibration on a probability scale.

A major criticism of the Bayesian model selection approach is that the choice of prior parameter distribution  $\pi(\boldsymbol{\theta}_i | M_i)$  can have a considerable impact on the posterior probabilities in (17) (see for instance Lindley, 1957; Kass and Raftery, 1995; Berger and Pericchi, 1996 and many other references in Vanpaemel, 2010). For our particular application, two “default” priors are evaluated in S5: (1) a noninformative but proper prior, and (2) the overly informative prior of Aitkin (1991) which effectively uses the data twice. Both are found to emphatically select the GLE-200 model, regardless of the true model which is used to simulate the data.

Fortunately, another default prior construction is available for the multiply replicated experiment at hand. That is, priors for the 10 “testing” datasets retained for model comparison in Figure 2 can be obtained by pooling the remaining 66 “training” datasets through the use of a hierarchical model. Specifically, for each model  $M_i$ , the hierarchical model on all  $m = 76$  datasets  $\mathbf{x}_1, \dots, \mathbf{x}_m$  is

$$(18) \quad \mathbf{x}_j | \boldsymbol{\theta}_j \stackrel{\text{ind}}{\sim} f(\mathbf{x}_j | \boldsymbol{\theta}_j), \quad \boldsymbol{\theta}_j \stackrel{\text{iid}}{\sim} g(\boldsymbol{\theta} | \boldsymbol{\eta}), \quad \boldsymbol{\eta} \sim \pi(\boldsymbol{\eta}),$$

where we have dropped the dependence on  $M_i$  to simplify notation. In our context,  $f(\mathbf{x} | \boldsymbol{\theta})$  are multivariate Normal densities corresponding to individual fBM or GLE models for each particle trajectory ( $\boldsymbol{\theta}_{\text{fBM}} = (\mu, \sigma, H)$  and  $\boldsymbol{\theta}_{\text{GLE}} = (\rho, \tau_1, \sigma)$ ). The hierarchical model naturally induces heterogeneity in these trajectories, which in turn can account for the ergodicity breaking phenomenon described in Section 1.2. Fitting (18) to the  $t = 66$  training datasets  $\mathbf{x}_{\text{train}} = (\mathbf{x}_1, \dots, \mathbf{x}_t)$  produces a posterior distribution

$$(19) \quad \begin{aligned} p(\boldsymbol{\eta} | \mathbf{x}_{\text{train}}) &\propto \pi(\boldsymbol{\eta}) \prod_{j=1}^t p(\mathbf{x}_j | \boldsymbol{\eta}) \\ &= \pi(\boldsymbol{\eta}) \prod_{j=1}^t \int f(\mathbf{x}_j | \boldsymbol{\theta}) g(\boldsymbol{\theta} | \boldsymbol{\eta}) d\boldsymbol{\theta}. \end{aligned}$$

A proper parameter prior for the 10 testing datasets  $\mathbf{x}_{\text{test}} = (\mathbf{x}_{t+1}, \dots, \mathbf{x}_m)$  in Figure 2 is then

$$(20) \quad \pi_{\text{test}}(\boldsymbol{\theta}) = \int g(\boldsymbol{\theta} | \boldsymbol{\eta}) p(\boldsymbol{\eta} | \mathbf{x}_{\text{train}}) d\boldsymbol{\eta}.$$

This approach to prior specification for Bayesian model comparisons is an instance of the *intrinsic Bayes factor* procedure described by Berger and Pericchi (1996).

**4.1. Approximate Fitting of the Hierarchical Model.** While the prior  $\pi_{\text{test}}(\boldsymbol{\theta})$  in (20) is conceptually appealing, its estimation typically requires computationally intensive Markov chain Monte Carlo (MCMC) techniques. As an alternative, we outline here an approximation which allows many of the calculations to be run in parallel, and which is generally applicable for approximate inference with hierarchical models.

1. We begin selecting a prior  $g_0(\boldsymbol{\theta})$  and obtaining posterior samples from

$$(21) \quad p_0(\boldsymbol{\theta}_j | \mathbf{x}_j) \propto f(\mathbf{x}_j | \boldsymbol{\theta}_j) g_0(\boldsymbol{\theta}_j)$$

independently for each training set  $\mathbf{x}_1, \dots, \mathbf{x}_t$ . Any  $g_0(\boldsymbol{\theta})$  can be used, as long as it is the same prior for each  $\mathbf{x}_j$ . In our case,  $g_0(\boldsymbol{\theta})$  were the improper priors (13) and (15) defined in Section 3.2. This stage can be implemented in parallel as the inference for each dataset is independent from any other.

2. Let’s suppose that each posterior  $p_0(\boldsymbol{\theta}_j | \mathbf{x}_j)$  is approximately Normal:

$$(22) \quad p_0(\boldsymbol{\theta}_j | \mathbf{x}_j) \approx \exp \left\{ -\frac{1}{2}(\boldsymbol{\theta}_j - \boldsymbol{\lambda}_j)' \boldsymbol{\Omega}_j (\boldsymbol{\theta}_j - \boldsymbol{\lambda}_j) + \frac{1}{2} \log |\boldsymbol{\Omega}_j| \right\}.$$

We now consider a prior on the random effects  $\Theta = (\theta_1, \dots, \theta_t)$  for each training set of the form

$$p(\Theta | \lambda_0, \Omega_0) \propto \prod_{j=1}^t \exp \left\{ -\frac{1}{2}(\theta_j - \lambda_0)' \Omega_0 (\theta_j - \lambda_0) + \log g_0(\theta_j) \right\}.$$

Then for a given prior  $\pi(\lambda_0, \Omega_0)$  on the hyperparameters  $\eta = (\lambda_0, \Omega_0)$ , the posterior distribution of all parameters  $(\Theta, \lambda_0, \Omega_0)$  is approximately

$$(23) \quad \begin{aligned} p(\Theta, \lambda_0, \Omega_0 | \mathbf{x}_{\text{train}}) &\propto \pi(\lambda_0, \Omega_0) \times p(\Theta | \lambda_0, \Omega_0) \times \prod_{j=1}^t f(\mathbf{x}_j | \theta_j) \\ &\approx \pi(\lambda_0, \Omega_0) \times \\ &\quad \exp \left\{ -\frac{1}{2} \sum_{j=1}^t (\theta_j - \lambda_j)' \Omega_j (\theta_j - \lambda_j) + (\theta_j - \lambda_0)' \Omega_0 (\theta_j - \lambda_0) \right\}. \end{aligned}$$

3. The approximate posterior (23) has precisely the form of a multilevel Normal model, for which Bayesian inference can easily be conducted with the help of a Gibbs sampler. That is, for the noninformative scale-invariant hyperparameter prior

$$\pi(\lambda_0, \Omega_0) \propto |\Omega_0|^{(\alpha+d)/2-2},$$

the Gibbs sampler updates its various components using the analytical distributions

$$(24) \quad \begin{aligned} \theta_j | \lambda_0, \Omega_0, \mathbf{x}_{\text{train}} &\stackrel{\text{ind}}{\sim} \mathcal{N}_d \left( \mathbf{B}_j \lambda_0 + (\mathbf{I} - \mathbf{B}_j) \lambda_j, (\mathbf{I} - \mathbf{B}_j) \Omega_j^{-1} \right), \\ \Omega_0 | \theta, \mathbf{x}_{\text{train}} &\sim \mathcal{W}_d \left( \mathbf{S}^{-1}, \alpha \right), \\ \lambda_0 | \theta, \Omega_0, \mathbf{x}_{\text{train}} &\sim \mathcal{N}_d \left( \bar{\lambda}, \frac{1}{m} \Omega_0^{-1} \right) \end{aligned}$$

where  $\mathcal{W}_d(\Psi, \nu)$  denotes the Wishart distribution and

$$\mathbf{B}_j = \Omega_j^{-1} (\Omega_j^{-1} + \Omega_0^{-1})^{-1}, \quad \bar{\lambda} = \frac{1}{t} \sum_{j=1}^t \lambda_j, \quad \mathbf{S} = \sum_{j=1}^t (\lambda_j - \bar{\lambda})(\lambda_j - \bar{\lambda})'.$$

4. The Gibbs sampler (24) produces MCMC draws  $\eta^{(1)}, \eta^{(2)}, \dots$  from  $p(\eta | \mathbf{x}_{\text{train}})$ , where  $\eta^{(m)} = (\lambda_0^{(m)}, \Omega_0^{(m)})$ . Our goal is to produce draws from  $\pi_{\text{test}}(\theta)$  in (20). If the independent inference prior in (21) is  $g_0(\theta) \propto 1$ , then posterior draws from  $p(\eta | \mathbf{x}_{\text{train}})$  can directly be combined with draws from

$$(25) \quad \theta^{(m)} | \lambda_0^{(m)}, \Omega_0^{(m)} \sim \mathcal{N} \left( \lambda_0^{(m)}, [\Omega_0^{(m)}]^{-1} \right)$$

to produce samples from  $\pi_{\text{test}}(\theta)$ . Otherwise, the  $\theta^{(m)}$  from (25) can serve as proposals for an Importance sampler with weights  $w_m \propto g_0(\theta^{(m)})$ .

5. Finally, the samples from  $\pi_{\text{test}}(\theta)$  were used to approximate  $\pi_{\text{test}}(\theta)$  by the best fitting conjugate priors (11) and (14). This proved to be a very minor adjustment in our situation, but with considerable benefits in computational tractability.

An attractive feature of the approximate hierarchical model above is that the bulk of its calculations – fitting each  $p(\theta_j | x_j)$  – can be conducted in parallel. A similar approach was adopted by Lunn et al. (2013) to fit the hierarchical model exactly, employing a Metropolis-Hastings re-sampling step for the conditional draws from  $p(\theta_j | \lambda_0, \Omega_0, x_{\text{train}})$ . A potential drawback of this exact MCMC algorithm is that the Metropolis-Hastings acceptance rates are adversely affected in situations where the independent posteriors are pooled heavily towards the common mean.

To improve the accuracy of the Normal approximation (22), we transformed the parameters to  $\theta_{\text{fBM}} = (\mu, \log(\sigma^2), H)$  and  $\theta_{\text{GLE}} = (v/\rho, v, \log(\sigma^2))$ . Figure 6 displays the 2D contours of  $\pi_{\text{test}}(\theta)$  for the fBM and GLE-200 models under the normalizing transformations.

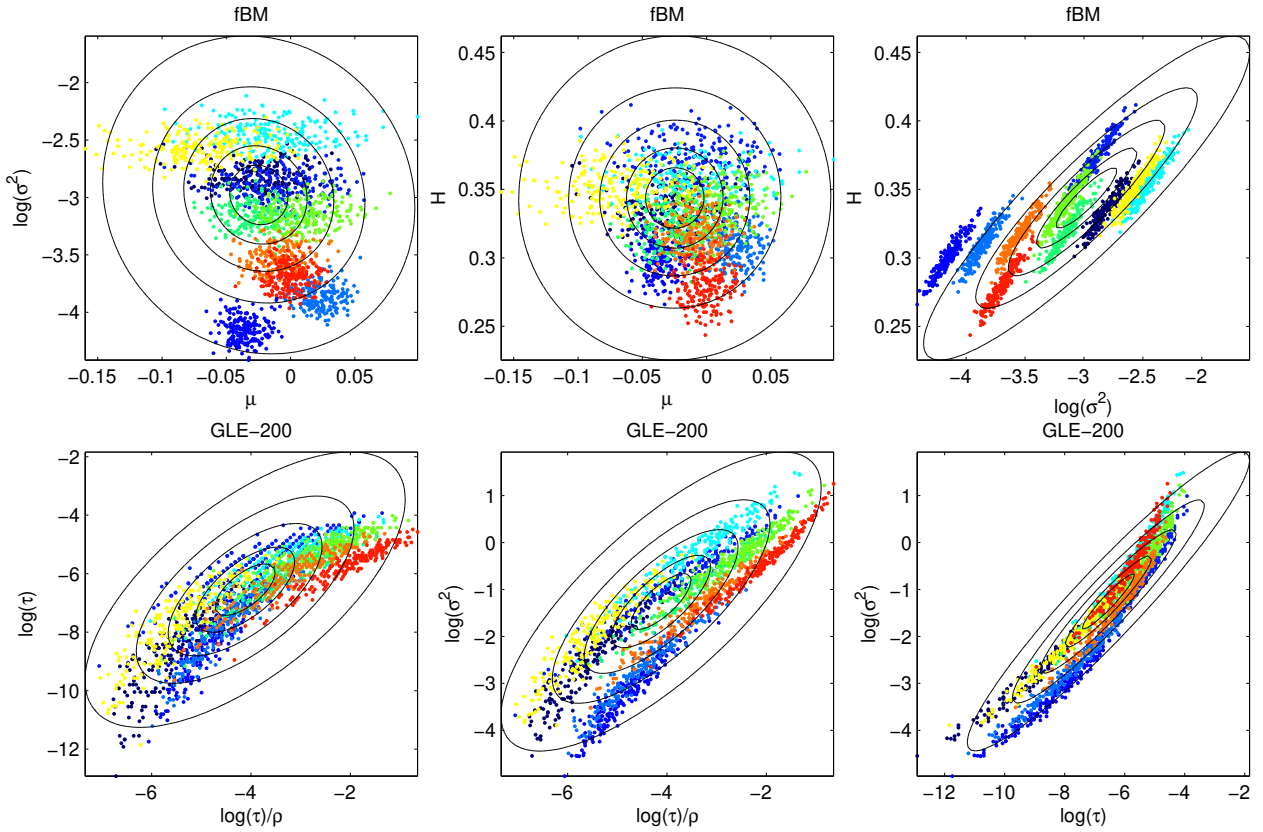


FIGURE 6. Prior from the approximate hierarchical model fitted to the  $t = 66$  training datasets. The black contour lines correspond to  $Q = 10, 25, 50, 75, 95\%$  quantiles of the  $\pi_{\text{test}}(\theta)$  prior. In color are sample points from the original posteriors  $p_0(\theta | x)$  of the test data from Figure 2.

**4.2. Model Comparison Results.** The data-driven priors  $\pi_{\text{test}}(\theta_i | M_i)$  yield marginal data densities

$$(26) \quad f_i(x) = \int p(x | \theta_i, M_i) \pi_{\text{test}}(\theta_i | M_i) d\theta_i.$$

By approximating  $\pi_{\text{test}}(\boldsymbol{\theta}_i | M_i)$  with a conjugate form, we were able to reduce the 3-dimensional parameter integrals in (26) by 1- and 2-dimensional deterministic calculations for the fBM and GLE models respectively.

To evaluate the performance of the hierarchical model prior, 1000 datasets from each of three models – fBM, GLE-200, and GLE-4 – were simulated with parameters drawn from  $\pi_{\text{test}}(\boldsymbol{\theta}_i | M_i)$ . The posterior probabilities  $p(M_i | \mathbf{x})$  were calculated for each dataset and two-way comparison between models. Histograms of these probabilities are displayed in Figures 7-9. The dotted red line indicates the median posterior probability for the “true” model under which we simulated the data. This probability was highest when comparing fBM to GLE-4 (around 85%), and lowest when comparing GLE-200 to GLE-4 (around 70%).

The probability of reporting a posterior probability value less than 50%,

$$\text{Prob}(p(M_i | \mathbf{x}) < .5 | M_i),$$

corresponds to the area in the yellow histogram bars, and is reported in the boxes in Figures 7-9. These values indicate that the classification rule which selects the model with higher posterior probability has a worst-case error rate of about 30% (the probability of incorrectly selecting GLE-4 instead of GLE-200).

We now turn to the 10 testing datasets of Figure 2. The posterior probabilities for these data are displayed in Tables 1-3. Also displayed is the following measure of uncertainty associated with the selection of a particular model. Let

$$\alpha = \alpha(\mathbf{x}) = \max \{p(M_1 | \mathbf{x}), p(M_2 | \mathbf{x})\}$$

be the posterior probability of the more likely between two models  $M_1$  and  $M_2$ . If we must select between these two models, presumably we will pick the one with the largest posterior probability. Let  $M_0$  denote the model we have selected and  $M_A$  denote the other model (i.e., the alternative). Then for a given dataset  $\mathbf{x}_{\text{obs}}$ , the probability

$$(27) \quad \beta = \text{Prob}(\alpha > \alpha_{\text{obs}} | M_A)$$

is the fraction of datasets under  $M_A$  which would have been more in favor of  $M_0$  than the observed data  $\mathbf{x}_{\text{obs}}$ . The higher this value, the higher the uncertainty about the selected model, as this indicates a higher probability of finding more evidence in favor of  $M_0$  even though  $M_A$  is true. We refer to (27) as the “missclassification uncertainty” and report its value in Tables 1-3. Based on these tables we make the following observations: (1) the datasets express little preference between the fBM and GLE-200 models; and (2) both fBM and GLE-200 models are highly favored by the data against GLE-4. Both of these observations confirm the strong presence of subdiffusion in the particle trajectories on the experimental time scale.

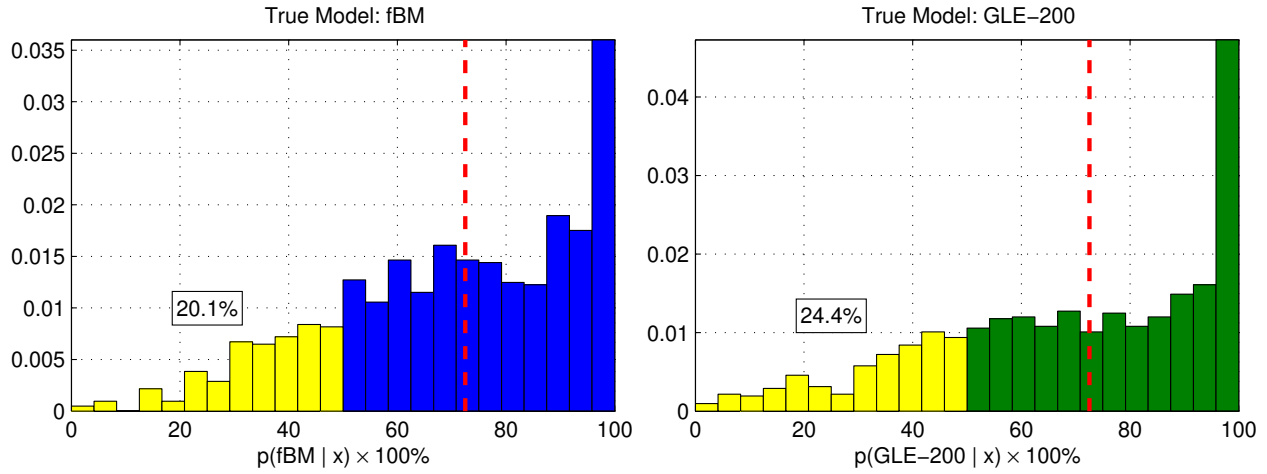


FIGURE 7. Posterior probability using simulated data for fBM vs. GLE-200.

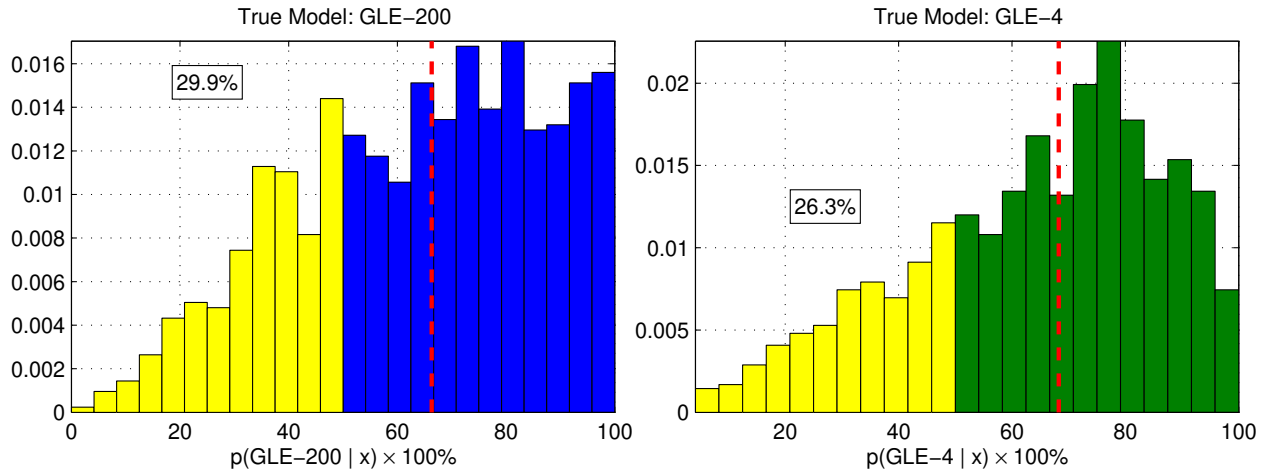


FIGURE 8. Posterior probability using simulated data for GLE-200 vs. GLE-4.

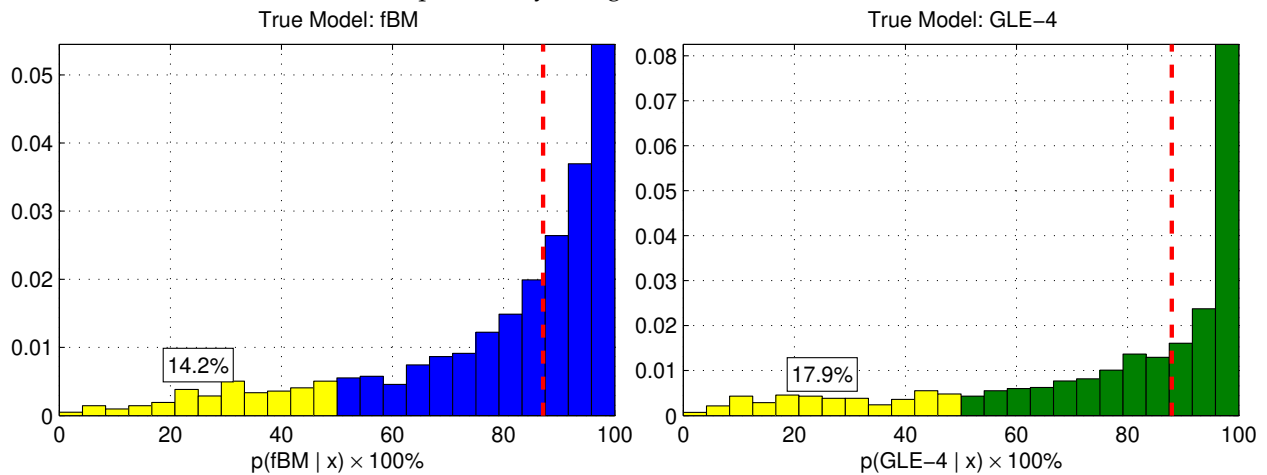


FIGURE 9. Posterior probability using simulated data for fBM vs. GLE-4.

Dataset	1	2	3	4	5	6	7	8	9	10
$\alpha$ (%)	55.3	86.3	<b>62.9</b>	50.5	<b>74</b>	<b>57</b>	<b>91.2</b>	74.9	<b>59.6</b>	<b>93.3</b>
$\beta$ (%)	19.1	2.6	10	24.2	3.7	14.6	0.6	6.5	12.2	0.2

TABLE 1. Posterior probability using the actual data for GLE-200 vs. fBM. Boldface values indicate that the model comparison favors GLE-200.

Dataset	1	2	3	4	5	6	7	8	9	10
$\alpha$ (%)	<b>74.2</b>	<b>95.8</b>	<b>69.2</b>	<b>80.8</b>	<b>86.2</b>	52.4	61.3	<b>78.8</b>	<b>76</b>	<b>50.8</b>
$\beta$ (%)	6.8	0	9.6	3.7	1.8	26.5	16.7	4.4	5.6	25.3

TABLE 2. Posterior probability using the actual data for GLE-200 vs. GLE-4. Boldface values indicate that the model comparison favors the GLE-200.

Dataset	1	2	3	4	5	6	7	8	9	10
$\alpha$ (%)	<b>78</b>	<b>99.3</b>	<b>56.9</b>	<b>81.1</b>	<b>68.6</b>	59.3	94.2	<b>91.7</b>	<b>68.2</b>	93.1
$\beta$ (%)	6.8	0	14.4	5.3	10.1	9.9	0.4	1.2	10.3	0.4

TABLE 3. Posterior probability using the actual data for fBM vs. GLE-4. Boldface values indicate that the model comparison favors fBM.

## 5. GOODNESS-OF-FIT

While the comparisons in the previous section express a preference for two of the candidate models, they do not attest to the quality of the models' fit to the observed data. In this section, we shall employ the models to make various predictions of scientific interest and compare them to empirical findings.

**5.1. Ergodicity Breaking.** We have seen in Figure 1 that the 76 experimental particle trajectories are considerably more heterogeneous than a single fBM or GLE model would predict. Figure 10 displays the pathwise MSD curves for real and simulated data from the models  $f(x|\theta)$ , but with a distribution of parameters,  $\pi(\theta)$ . We take this distribution to be the posterior distributions  $\pi(\theta) = \pi_{\text{test}}(\theta)$  obtained in Section 3. All models exhibit a range of pathwise MSDs which is comparable to that of the empirical data. This demonstrates that hierarchical modeling can be used to capture the phenomenon of ergodicity breaking – a central feature of the CTRW model mentioned in Section 1.2.

**5.2. Short- and Long-Term Effects.** The following calculations are for the first dataset DS-1 in Figure 2; results on the other nine test sets were very similar. We use several second-order properties of the models to see whether they capture short-term and long-term effects. In Figure 11, we compare the empirical variance and autocorrelation against our models' predictions. These were obtained from simulated data from the predictive distribution  $p(x|x_{\text{DS-1}}) =$

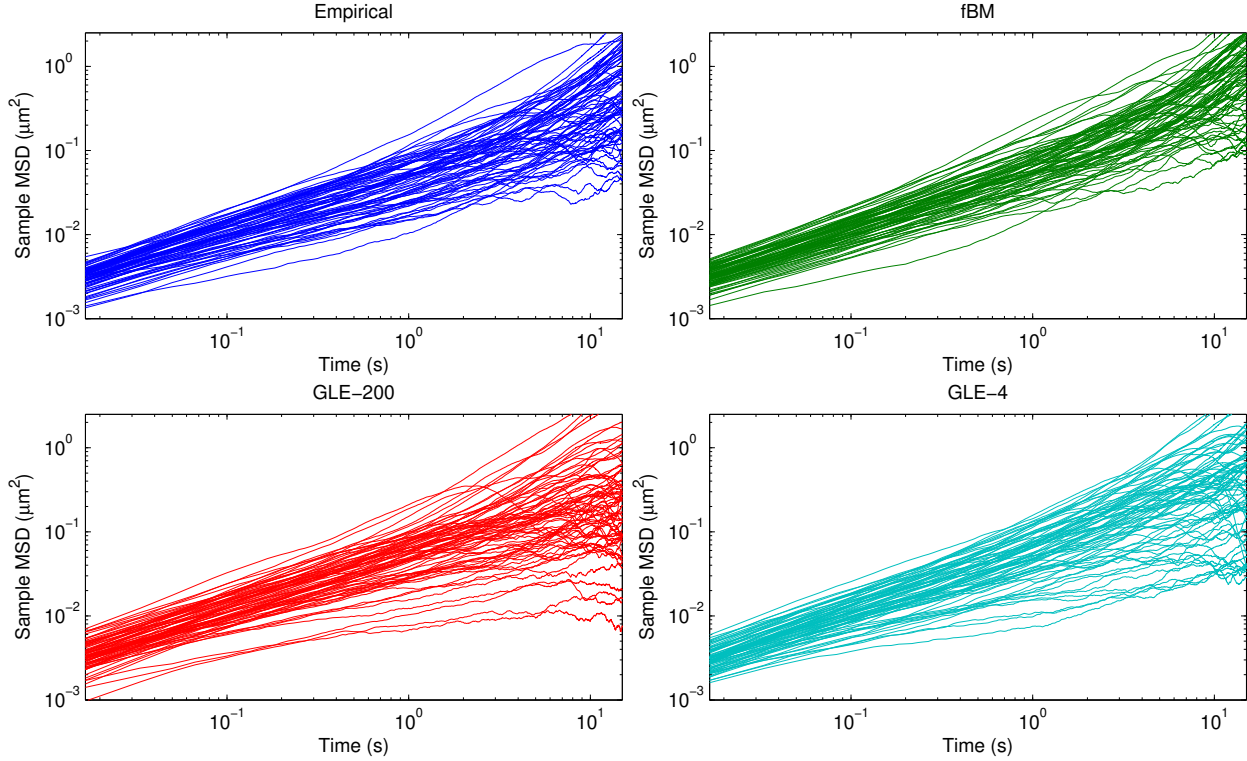


FIGURE 10. Ergodicity breaking, heterogeneous models.

$\int p(x | \theta) p(\theta | x_{\text{DS-1}}) d\theta$ . None of the three models can be rejected based on autocorrelations up to lag 10.

For long-term effects, we consider the (local) Whittle estimator  $\hat{\alpha}_W$  of the subdiffusion parameter  $\alpha$ . The exact calculation is outlined in [Robinson \(1995\)](#) and we have used  $m = 450$  periodogram frequencies.

It is well-known that the Whittle estimator  $\hat{\alpha}_W$  has appreciable bias at the sample sizes which were available to us (see for instance [Andrews and Sun, 2004](#)). It is, however, a model-free heuristic which can be employed for posterior predictive checks. Figure 12 indicates good agreement between the Whittle estimators calculated on data simulated from the model and the empirical value calculated on DS-1. For the fBM and GLE-200 models, we note the slight discrepancy between the model-free estimate  $\hat{\alpha}_W$  and the model-dependent estimates of  $\alpha$ , the posterior means  $\mathbb{E}[2H | x]$  and  $\mathbb{E}[1/\rho | x]$ .

**5.3. Exact Model Residuals.** The previous goodness-of-fit tests suggest that our models adequately describe several key properties of the empirical data. It could be argued, however, that these tests are fairly weak, since our test statistics have considerable variability over the simulated data. Indeed, none of the tests above provide evidence against the fit of the GLE-4 model, despite the analysis in Section 4 suggesting that GLE-4 is considerably worse than the other two models in a relative sense. Here we present a very powerful test against our models by considering the following collection of model residuals.

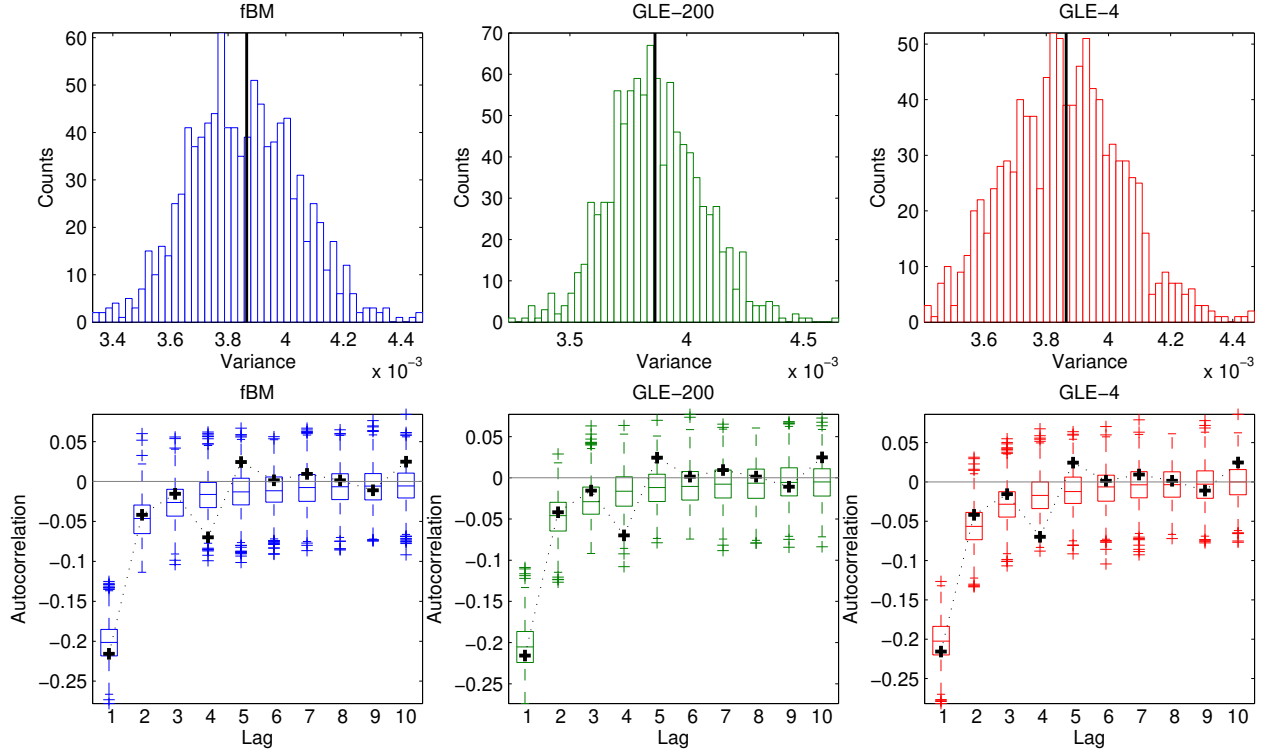


FIGURE 11. Sample variances and autocorrelations for simulated data from each model. Empirical estimates are in black.

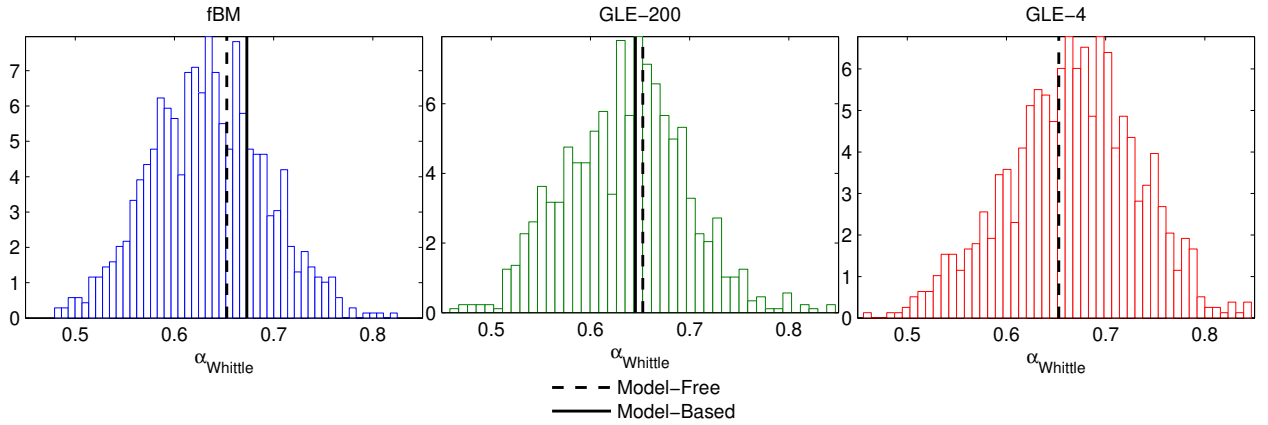


FIGURE 12. Whittle estimator of the subdiffusion coefficient  $\alpha$ . The dotted line indicates the sample value of these estimates for DS-1. The histograms display the dispersion of these estimates over the simulated data. The black lines correspond to model-dependent estimates of  $\alpha$ . For fBM this is  $\hat{\alpha}_W = \mathbb{E}[2H | x]$  and for GLE-200 this is  $\hat{\alpha}_W = \mathbb{E}[1/\rho | x]$ .

We begin with an assumption that the distribution of the testing data  $x$  is full specified by model  $M_i$ :

$$H_0 : x | M_i \sim f_i(x),$$

where  $f_i(x) = \int f(x | \theta_i, M_i) \pi_{\text{test}}(\theta_i | M_i) d\theta_i$  is the marginal data distribution (26) derived in Section 4. Then under  $H_0$ , the  $N = 1798$  observed increments  $\mathbf{x} = (x_1, \dots, x_N)$  can be converted to iid Uniforms by the so-called Rosenblatt transformation (Rosenblatt, 1952). That is, let  $\mathbf{U} = (U_1, \dots, U_N)$ , where each  $U_n$  corresponds to the quantile of  $x_n$  in its 1-step predictive distribution,  $p(x_n | x_{n-1}, \dots, x_1)$ . Then  $U_n \stackrel{\text{iid}}{\sim} \text{Unif}(0, 1)$ .

Since  $f_i(x)$  is not available in closed-form, we extract the ‘‘Rosenblatt residuals’’ from  $f_i(x)$  by the following calculation. For each  $1 \leq n \leq N$ :

1. Sample  $\theta^{(1)}, \dots, \theta^{(M)}$  from the posterior distribution

$$p(\theta | x_1, \dots, x_{n-1}) \propto L(\theta | x_1, \dots, x_{n-1}) \pi_{\text{test}}(\theta).$$

2. Sample each  $x_n^{(1)}, \dots, x_n^{(M)}$  independently from the conditional distributions

$$x_n^{(m)} | \theta^{(m)} \stackrel{\text{ind}}{\sim} p(\cdot | x_1, \dots, x_{n-1}, \theta^{(m)}).$$

A computationally efficient method which minimizes the Monte Carlo error in steps 1 and 2 is presented in S2.3.

3. Calculate  $U_n = \frac{1}{M} \sum_{m=1}^M \delta\{x_n^{(m)} \leq x_n^{\text{obs}}\}$ , where  $x_n^{\text{obs}}$  is the observed value from the actual data.

The Rosenblatt residuals for the best-fitting dataset to each of our models are displayed in the QQ plots at the bottom of Figure 13. These datasets are DS-2 for fBM, DS-5 for GLE-200, and DS-7 for GLE-4. For a more conventional display, the residuals have been converted to z-scores,  $Z_n = \Phi^{-1}(U_n)$ , where  $\Phi$  is the CDF of a standard Normal.

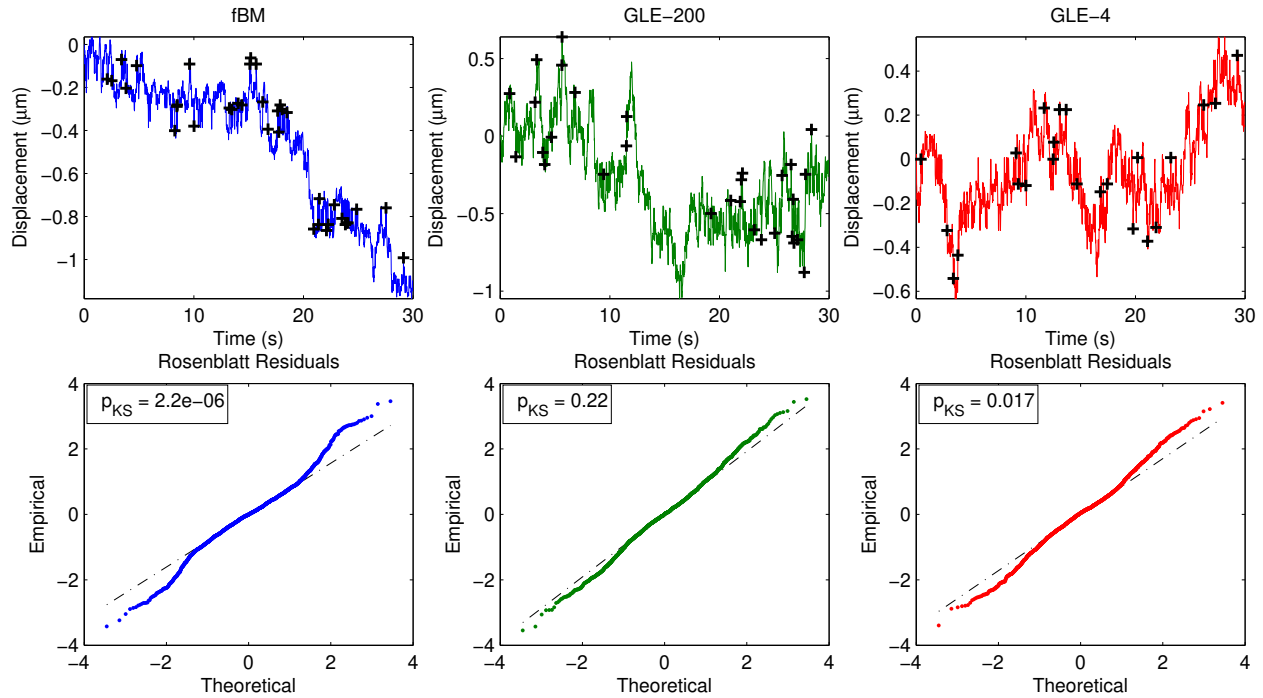


FIGURE 13. Rosenblatt residuals for the best-fitting dataset to each of three models. The crosses in the top row correspond to the 1% most extreme model outliers.

Qualitatively, the model residuals have heavier tails than expected under  $H_0$ . The 1% of most severe model outliers are displayed as crosses in the top row of Figure 13. It is interesting to note that these extreme values often but don't always coincide with large jumps in the particle trajectories. Also displayed in Figure 13 are p-values for the Kolmogorov-Smirnov Normality test. Given its high sensitivity, it is rather surprising that the Kolmogorov-Smirnov test fails to reject the GLE-200 model at the 5% nominal level.

## 6. DISCUSSION

In this article we have detailed an analysis of several models for tracer particle diffusion in biological fluids. The candidate models were fBM and a zero-mass GLE with generalized Rouse spectrum for the relaxation times with  $K = 4$  and  $K = 200$  modes. Model comparisons taking advantage of complete information contained in the observed likelihood were performed using intrinsic Bayes factors. This obviates the need for heavily relying on summary statistics such as the MSD. The proper parameter priors were naturally constructed by dividing the data into training and test sets and pooled through a hierarchical model. We employed a Normal approximation to greatly accelerate computations for this model by allowing most of the inference to be performed in parallel. This technique is broadly applicable for approximate inference with other complex hierarchical models such as ours.

The posterior model probabilities revealed a similar degree of fit between fBM and the GLE model with  $K = 200$  modes, with both models displaying a markedly superior agreement with the data than the GLE with only  $K = 4$  modes. As  $K \rightarrow \infty$ , the fBM and GLE models behave identically at intermediate timescales but differently at both short and long range. The agreement between fBM and GLE-200 is further evidence of the strong presence of subdiffusive behavior on the experimental timescale. While the GLE-200 model is directly based on viscoelastic diffusion theory, the fBM model has one less "non least-squares" parameter (see S2) and is thus easier to fit. The agreement between the two models and particularly Figure 5 suggest that if the objective is to estimate the subdiffusion coefficient  $\alpha$ , fBM is a good proxy for GLE-200 on our experimental timescale.

Goodness-of-fit for all three candidate models was assessed using several criteria. A particularly stringent test involved the models' Rosenblatt residuals, which for our data were obtained by applying the probability integral transform to the one-step predictive distributions. The residuals exhibited heavier tails than expected under the null. Our investigations suggest that this is not due to a failure of the models to capture short- or long-range dynamics, but rather to particle confinement not adequately described by a Gaussian model.

While our candidate models are fully specified in continuous time, exhibit anomalous subdiffusion, ergodicity breaking, and cannot be rejected based on various second-order test statistics, our analysis largely confirms that modeling of tracer bead displacement in pulmonary mucus has considerable room for improvement. One approach to account for the particle trapping we

have observed is via regime-switching models (e.g. [Kim and Nelson, 1999](#)). For example, the fBM parameters might depend on time and/or location in order to account for caging and/or binding events.

Another important open question relates to the sensitivity of the first-passage time calculations to the choice of model. It would be interesting to measure the discrepancy between such predictions for the fBM and GLE-200 models well beyond the experimental timescale. However, to empirically assess the validity of such predictions, it is necessary to increase the observation period by an order of magnitude or more. This is rather delicate with the current experimental setup, as the tracer particles tend to move out of the camera's range given a sufficient amount of time. It is possible to restrict attention to only particles that remain in range for the duration of the experiment, but then inference must be conducted by conditioning on this fact. We are actively looking into this approach as well as different experimental tracking strategies.

## SUPPLEMENTARY MATERIAL

### S1. SUBDIFFUSIVE BEHAVIOR OF THE GLE WITH ROUSE SPECTRUM KERNEL

**S1.1. Asymptotically Subdiffusive Behavior in the Zero Mass Limit.** Suppose that  $X(t)$  is the displacement of a particle of which the velocity  $V(t)$  obeys the GLE

$$(S1) \quad m\dot{V}(t) = - \int_{-\infty}^t \gamma(t-s)V(s) ds + F(t),$$

where

$$\langle F(t), F(s) \rangle = k_B T \gamma(t-s).$$

Assuming that a stationary solution to (S1) exists, the process  $X(t) := \int_0^t V(s) ds$  is well-defined by the Fourier transform:

$$\tilde{X}(\omega) = \frac{\tilde{V}(\omega)}{2\pi i \omega},$$

where the Fourier transform  $\tilde{x}(\omega)$  of any stationary process  $x(t)$  can be defined (e.g., [Brockwell and Davis, 2009](#)) such that

$$x(t) = \int_{-\infty}^{\infty} e^{-2\pi i t \omega} d\tilde{x}(\omega).$$

Moreover, if  $\Gamma(t) = \langle X^2(t) \rangle$  is the MSD of  $X(t)$  and  $\alpha(t)$  is the autocorrelation of  $V(t)$ , then

$$\tilde{\Gamma}(\omega) = \frac{\tilde{\alpha}(\omega)}{(2\pi\omega)^2}.$$

By multiplying each side of (S1) by  $V(0)$  and taking expectations, since  $V(0)$  and  $F(t)$  are uncorrelated we obtain

$$m\alpha'(t) = - \int_{-\infty}^t \gamma(t-s)\alpha(s) ds.$$

Since  $\alpha(t)$  is a real symmetric function, its Fourier transform is bijective with a Laplace transform, such that

$$\tilde{\alpha}(\omega) = \hat{\alpha}(|s|) - \alpha(0),$$

where  $s = 2\pi i\omega$  and the Laplace transform is

$$\hat{\alpha}(s) = \lim_{\epsilon \downarrow 0} \int_{-\epsilon}^{\infty} e^{-st} \alpha(t) dt.$$

The Laplace transform of  $\alpha(t)$  is (Kneller, 2011):

$$\hat{\alpha}(s) = \frac{\mathbb{E}[V(0)^2]}{s + \hat{\gamma}(s)/m} = \frac{m\mathbb{E}[V(0)^2]}{ms + \hat{\gamma}(s)} \sim \frac{1}{\hat{\gamma}(s)}$$

for  $s \sim 0$  in the zero-mass limit as  $m \rightarrow 0$ . Therefore, a power law decay in the thermal force autocorrelation

$$\langle F(0), F(t) \rangle \sim t^{-\alpha}$$

for  $t \rightarrow \infty$  and  $0 < \alpha < 1$  implies that

$$\hat{\alpha}(s) \sim s^{1-\alpha} \quad \Longrightarrow \quad \tilde{\Gamma}(\omega) \sim \frac{1}{\omega^{\alpha+1}}$$

for  $s \sim 0$ , which results in asymptotically subdiffusive behavior:

$$\Gamma(t) = \langle X^2(t) \rangle \sim t^\alpha, \quad t \rightarrow \infty.$$

**S1.2. Convergence of the Prony Series Kernel.** Define the function

$$(S2) \quad K(t; \alpha) := \alpha t^{-\alpha} \gamma(t; \alpha)$$

where  $\gamma$  is the incomplete Gamma function,  $\gamma(t; \alpha) := \int_0^t y^{\alpha-1} e^{-y} dy$ . Note that  $\gamma(t; \alpha)$  is a slowly-varying function in  $t$ , and therefore  $K(t; \alpha) \sim t^{-\alpha}$  as  $t \rightarrow \infty$  by the result of Kneller (2011). By the following proposition, we establish the convergence of our Prony series kernel to  $K(t; \alpha)$ , thereby obtaining asymptotically subdiffusive behavior  $\langle X^2(t) \rangle \sim t^\alpha$ .

**Proposition S1.1.** *Let  $K_N(t; \tau_1, \rho)$  be a Prony series kernel (7), defined with the Generalized Rouse spectrum (8) that has smallest relaxation time  $\tau_1$  and shape parameter  $\rho$ :*

$$K_N(t; \tau_1, \rho) = \frac{1}{N} \sum_{n=1}^N \exp\left(-\frac{t}{\tau_1} \left(\frac{n}{N}\right)^\rho\right).$$

Then

$$(S3) \quad \lim_{N \rightarrow \infty} \sup_{t \geq 0} \left| K_N(t; \tau_1, \rho) - K\left(\frac{t}{\tau_1}; \frac{1}{\rho}\right) \right| = 0$$

*Proof.* First we note that taking the substitution  $y = tx^\rho/\tau_1$  we can establish the identity,

$$\int_0^t \exp\left(-\frac{t}{\tau_1} x^\rho\right) dx = \frac{1}{\rho} \left(\frac{t}{\tau_1}\right)^{-\frac{1}{\rho}} \int_0^{\frac{t}{\tau_1}} y^{\frac{1}{\rho}-1} e^{-y} dy = K\left(\frac{t}{\tau_1}; \frac{1}{\rho}\right)$$

Pointwise convergence follows from the Riemann approximation, and the uniform convergence in  $t$  follows because the exponential is decreasing and concave up:

$$\begin{aligned}
& |K_N(t) - K(t\tau_1^{-1}; \rho^{-1})| \\
&= \left| \int_0^1 \exp\left(-\frac{t}{\tau_1} x^\rho\right) - \frac{1}{N} \sum_{n=1}^N \exp\left(-\frac{t}{\tau_1} \left(\frac{n}{N}\right)^\rho\right) \right| \\
&\leq \frac{1}{2N} \sum_{n=1}^N \exp\left(-\frac{t}{\tau_1} \left(\frac{n-1}{N}\right)^\rho\right) - \exp\left(-\frac{t}{\tau_1} \left(\frac{n}{N}\right)^\rho\right) \\
&\leq \frac{1}{2N} \left(1 - e^{-\frac{t}{\tau_1}}\right) \leq \frac{1}{2N}.
\end{aligned}$$

Taking the limit as  $N \rightarrow \infty$  yields the claim.  $\square$

## S2. MARGINALIZATION OF REGRESSION PARAMETERS IN GAUSSIAN MODELS

The fBM and GLE models (3) and (9) both have likelihoods which can be written in linear regression form

$$(S4) \quad \ell(\boldsymbol{\beta}, \sigma, \boldsymbol{\theta} | \mathbf{Y}) = -\frac{1}{2} \left( \frac{(\mathbf{Y} - \mathbf{X}\boldsymbol{\beta})' \mathbf{V}_\theta^{-1} (\mathbf{Y} - \mathbf{X}\boldsymbol{\beta})}{\sigma^2} + n \log(\sigma^2) + \log(|\mathbf{V}_\theta|) \right).$$

That is, for both models we have  $\mathbf{Y} := \mathbf{x} = (x_1, \dots, x_N)$ , the stationary increments. For fBM, we have  $\boldsymbol{\beta} = \mu$ ,  $\mathbf{X} = (\Delta t, \dots, \Delta t)$ , and  $\boldsymbol{\theta} = H$ , such that  $\mathbf{V}_\theta = V_H$  is a function of  $H$ . For the GLE model, there is no  $\mathbf{X}$  or  $\boldsymbol{\beta}$  and  $\boldsymbol{\theta} = (\rho, \tau_1)$ . Posterior inference with the regression model (S4) has the computational advantage of admitting analytical marginal inference via  $p(\boldsymbol{\theta} | \mathbf{Y})$ .

**S2.1. Marginal Posteriors.** Let  $d$  be the number of columns of  $\mathbf{X}$  and for given  $\boldsymbol{\theta}$ , consider the block matrix

$$[\mathbf{Y}\mathbf{X}]' \mathbf{V}^{-1} [\mathbf{Y}\mathbf{X}] = \mathbf{R}_{d+1 \times d+1} = \begin{pmatrix} s & \mathbf{U}' \\ \mathbf{U} & \mathbf{T} \end{pmatrix},$$

where  $s_{1 \times 1} = s_\theta$ ,  $\mathbf{U}_{d \times 1} = \mathbf{U}_\theta$ , and  $\mathbf{T}_{d \times d} = \mathbf{T}_\theta$  all depend on  $\boldsymbol{\theta}$ . The conjugate prior  $\pi(\boldsymbol{\Theta})$  for  $\boldsymbol{\Theta} = (\boldsymbol{\beta}, \sigma^2, \boldsymbol{\theta})$  in (S4) is of the form

$$(S5) \quad \begin{aligned} \boldsymbol{\theta} &\sim \pi(\boldsymbol{\theta}) \\ \sigma^2 | \boldsymbol{\theta} &\sim \text{Inv-Gamma}(\alpha, \gamma) \sim \Lambda(\alpha, \gamma) (\sigma^2)^{-\alpha-1} \exp(-\gamma/\sigma^2) \\ \boldsymbol{\beta} | \sigma, \boldsymbol{\theta} &\sim \mathcal{N}_d(\boldsymbol{\lambda}, \sigma^2 \boldsymbol{\Omega}^{-1}), \end{aligned}$$

where  $\Lambda(\alpha, \gamma) = \gamma^\alpha / \Gamma(\alpha)$ . This results in the posterior distribution

$$(S6) \quad \begin{aligned} \boldsymbol{\theta} | \mathbf{Y} &\sim \pi(\boldsymbol{\theta}) \times \frac{\Lambda(\alpha, \gamma)}{\Lambda(\alpha + \frac{n}{2}, \gamma + \hat{\gamma})} \left( \frac{|\boldsymbol{\Omega}|}{|\mathbf{T} + \boldsymbol{\Omega}| |\mathbf{V}|} \right)^{1/2} \\ \sigma^2 | \boldsymbol{\theta}, \mathbf{Y} &\sim \text{Inv-Gamma} \left( \alpha + \frac{n}{2}, \gamma + \hat{\gamma} \right) \\ \boldsymbol{\beta} | \sigma, \boldsymbol{\theta}, \mathbf{Y} &\sim \mathcal{N}_d \left( \hat{\boldsymbol{\lambda}}, \sigma^2 (\mathbf{T} + \boldsymbol{\Omega})^{-1} \right), \end{aligned}$$

where

$$\hat{\lambda} = (\mathbf{T} + \mathbf{\Omega})^{-1}(\mathbf{U} + \mathbf{\Omega}\lambda), \quad \hat{\gamma} = \frac{1}{2}(s + \lambda' \mathbf{\Omega} \lambda - (\mathbf{U} + \mathbf{\Omega}\lambda)' \hat{\lambda}).$$

Note that while  $\boldsymbol{\theta}$  and  $(\boldsymbol{\beta}, \sigma)$  in (S5) are *a priori* independent, this is no longer true conditional on  $\mathbf{Y}$ , as  $\hat{\gamma} = \hat{\gamma}_{\boldsymbol{\theta}}$ ,  $\hat{\lambda} = \hat{\lambda}_{\boldsymbol{\theta}}$  and  $\mathbf{T} = \mathbf{T}_{\boldsymbol{\theta}}$  all implicitly depend on  $\boldsymbol{\theta}$ . Indeed, (S5) can easily be modified to reflect a dependence between  $\boldsymbol{\theta}$  and  $(\boldsymbol{\beta}, \sigma)$  by letting  $\alpha = \alpha_{\boldsymbol{\theta}}$ ,  $\gamma = \gamma_{\boldsymbol{\theta}}$ , and so on. Upon substituting these terms into (S6), the form of the posterior remains exactly the same. This is how we approximated the intrinsic prior  $\pi_{\text{test}}(\boldsymbol{\theta})$  in Section 4.

S2.1.1. *Noninformative prior.* A popular noninformative prior for  $\boldsymbol{\beta}$  and  $\sigma$  is of the form

$$\pi(\boldsymbol{\beta}, \sigma^2, \boldsymbol{\theta}) \propto \pi(\boldsymbol{\theta}) / \sigma^2.$$

For this choice of prior, (S6) simplifies to

$$\begin{aligned} \boldsymbol{\theta} | \mathbf{Y} &\sim \frac{\pi(\boldsymbol{\theta})}{(\hat{\gamma}^{n-d} |\mathbf{T}| |\mathbf{V}|)^{1/2}} \\ \sigma^2 | \boldsymbol{\theta}, \mathbf{Y} &\sim \text{Inv-Gamma}\left(\frac{n-d}{2}, \hat{\gamma}\right) \\ \boldsymbol{\beta} | \sigma, \boldsymbol{\theta}, \mathbf{Y} &\sim \mathcal{N}_d(\hat{\boldsymbol{\beta}}, \sigma^2 \mathbf{T}^{-1}), \end{aligned}$$

where  $\hat{\boldsymbol{\beta}} = \mathbf{T}^{-1} \mathbf{U}$  and  $\hat{\gamma} = \frac{1}{2}(s - \mathbf{U}' \hat{\boldsymbol{\beta}})$ .

S2.1.2. *No regressors.* For the GLE model with  $\mathbf{X}\boldsymbol{\beta} = 0$ , the posterior distribution becomes

$$\begin{aligned} \boldsymbol{\theta} | \mathbf{Y} &\sim \frac{\pi(\boldsymbol{\theta})}{(\hat{\gamma}^n |\mathbf{V}|)^{1/2}} \\ \sigma^2 | \boldsymbol{\theta}, \mathbf{Y} &\sim \text{Inv-Gamma}\left(\frac{n}{2}, \hat{\gamma}\right), \end{aligned}$$

where  $\hat{\gamma} = s/2$ .

**S2.2. Marginal Data Distributions.** If the conjugate prior distribution (S5) is proper, it is possible to define the marginal data density

$$p(\mathbf{Y}) = \int p(\mathbf{Y} | \boldsymbol{\Theta}) \pi(\boldsymbol{\Theta}) d\boldsymbol{\Theta},$$

which is required to calculate the posterior model probabilities in Section 4. To do this, note that  $p(\mathbf{Y}) = p(\mathbf{Y}, \boldsymbol{\Theta}) / p(\boldsymbol{\Theta} | \mathbf{Y})$  for any value of  $\boldsymbol{\Theta} = (\boldsymbol{\beta}, \sigma^2, \boldsymbol{\theta})$ . Thus, we have

$$\begin{aligned} \log(\pi(\boldsymbol{\beta}, \sigma, \boldsymbol{\theta})) &= \log(\pi(\boldsymbol{\theta})) + \alpha \log(\gamma) - \log(\Gamma(\alpha)) - (\alpha + 1) \log(\sigma^2) - \frac{\gamma}{\sigma^2} \\ &\quad - \frac{1}{2} \frac{(\boldsymbol{\beta} - \boldsymbol{\lambda})' \boldsymbol{\Omega} (\boldsymbol{\beta} - \boldsymbol{\lambda})}{\sigma^2} - \frac{d}{2} \log(\sigma^2) + \frac{1}{2} \log(|\boldsymbol{\Omega}|) - \frac{d}{2} \log(2\pi), \\ \log(p(\mathbf{Y} | \boldsymbol{\beta}, \sigma, \boldsymbol{\theta})) &= -\frac{1}{2} \frac{(\boldsymbol{\beta} - \hat{\boldsymbol{\beta}})' \mathbf{T} (\boldsymbol{\beta} - \hat{\boldsymbol{\beta}}) + 2\hat{\gamma}}{\sigma^2} - \frac{n}{2} \log(\sigma^2) - \frac{1}{2} \log(|\mathbf{V}|) - \frac{n}{2} \log(2\pi), \\ \log(p(\boldsymbol{\beta}, \sigma, \boldsymbol{\theta} | \mathbf{Y})) &= -K + \log \left\{ \pi(\boldsymbol{\theta}) \times \frac{\gamma^\alpha \Gamma(\alpha + \frac{n}{2})}{(\hat{\gamma} + \gamma)^{\alpha + n/2} \Gamma(\alpha)} \left( \frac{|\boldsymbol{\Omega}|}{|\mathbf{T} + \boldsymbol{\Omega}| |\mathbf{V}|} \right)^{1/2} \right\} \\ &\quad + (\alpha + \frac{n}{2}) \log(\hat{\gamma} + \gamma) - \log(\Gamma(\alpha + \frac{n}{2})) - (\alpha + \frac{n}{2} + 1) \log(\sigma^2) - \frac{\gamma + \hat{\gamma}}{\sigma^2} \\ &\quad - \frac{1}{2} \frac{(\boldsymbol{\beta} - \hat{\boldsymbol{\lambda}})' (\mathbf{T} + \boldsymbol{\Omega}) (\boldsymbol{\beta} - \hat{\boldsymbol{\lambda}})}{\sigma^2} - \frac{d}{2} \log(\sigma^2) + \frac{1}{2} \log(|\mathbf{T} + \boldsymbol{\Omega}|) - \frac{d}{2} \log(2\pi), \end{aligned}$$

where

$$\exp(K) = \int \pi(\boldsymbol{\theta}) \times \frac{\gamma^\alpha \Gamma(\alpha + \frac{n}{2})}{(\hat{\gamma} + \gamma)^{\alpha + n/2} \Gamma(\alpha)} \left( \frac{|\boldsymbol{\Omega}|}{|\mathbf{T} + \boldsymbol{\Omega}| |\mathbf{V}|} \right)^{1/2} d\boldsymbol{\theta},$$

and no term involving  $\boldsymbol{\Theta}$  may appear in the final expression for  $p(\mathbf{Y})$  – including  $\mathbf{V}_\theta, \mathbf{T}_\theta, \hat{\boldsymbol{\beta}}_\theta, \hat{\boldsymbol{\lambda}}_\theta$ , and  $\hat{\gamma}_\theta$ . Upon making the appropriate cancelations, we have

$$\log(p(\mathbf{Y})) = \log \left( \frac{p(\mathbf{Y}, \boldsymbol{\Theta})}{p(\boldsymbol{\Theta} | \mathbf{Y})} \right) = K - \frac{n}{2} \log(2\pi).$$

**S2.3. Rosenblatt Residuals.** For  $\mathbf{Y} = (y_1, \dots, y_n)$ ,  $\mathbf{X} = (\mathbf{X}_1, \dots, \mathbf{X}_n)'$  and a proper conjugate prior of the form (S5), the calculation of the  $j$ th Rosenblatt residual  $U_j$  described in Section 5 requires a Monte Carlo sample from

$$\begin{aligned} p(y_j | \mathbf{y}_{1:j-1}) &= \int p(y_j | \mathbf{y}_{1:j-1}, \boldsymbol{\Theta}) p(\boldsymbol{\Theta} | \mathbf{y}_{1:j-1}) d\boldsymbol{\Theta} \\ &= \int p(y_j | \mathbf{y}_{1:j-1}, \boldsymbol{\theta}) p(\boldsymbol{\theta} | \mathbf{y}_{1:j-1}) d\boldsymbol{\theta}, \end{aligned}$$

where  $\mathbf{y}_{1:m} = (y_1, \dots, y_m)$ . To do this, we first use conjugacy to obtain a Monte Carlo sample from  $p(\boldsymbol{\theta} | \mathbf{y}_{1:j-1})$ . We then combine each of these samples with an analytical draw from  $p(y_j | \mathbf{y}_{1:j-1}, \boldsymbol{\theta})$ . Indeed, note that

$$y_j | \mathbf{y}_{1:j-1}, \boldsymbol{\Theta} \sim \mathcal{N}(\hat{a}_j + \hat{x}_j \boldsymbol{\beta}, \sigma^2 \hat{V}_j),$$

where  $\mathbf{C} = (V_{j1}, \dots, V_{jj-1})$ ,  $\mathbf{W} = [\mathbf{V}]_{1 \leq i, k \leq j-1}$ , and

$$\hat{a}_j = \mathbf{C} \mathbf{W}^{-1} \mathbf{y}_{1:j-1}, \quad \hat{x}_j = \mathbf{X}_j - \mathbf{C} \mathbf{W}^{-1} \mathbf{X}_{1:j-1}, \quad \hat{V}_j = V_{jj} - \mathbf{C} \mathbf{W}^{-1} \mathbf{C}'.$$

Integrating over the conjugate distribution  $\pi(\boldsymbol{\beta} | \sigma, \boldsymbol{\theta})$  leads to

$$y_j | \mathbf{y}_{1:j-1}, \sigma, \boldsymbol{\theta} \sim \mathcal{N}(\hat{a}_j + \mathbf{X}_j \boldsymbol{\lambda}, \sigma^2 (\hat{V}_j + \mathbf{X}_j \boldsymbol{\Omega}^{-1} \mathbf{X}_j')).$$

To integrate over  $\pi(\sigma | \boldsymbol{\theta})$ , note that

$$\sigma^2 | \boldsymbol{\theta} \sim \text{Inv-Gamma}(\alpha, \gamma) \iff \frac{\sigma^2}{2\gamma} \sim \text{Inv-}\chi^2_{(2\alpha)}.$$

Therefore, if

$$z_j = \frac{y_j - \hat{a}_j - \mathbf{X}_j \boldsymbol{\lambda}}{\sqrt{\hat{V}_j + \mathbf{X}_j \boldsymbol{\Omega}^{-1} \mathbf{X}_j'}} \times \sqrt{\alpha/\gamma},$$

then  $z_j$  is a  $t$ -distributed random variable with  $2\alpha$  degrees of freedom,

$$z_j | \mathbf{y}_{1:j-1}, \boldsymbol{\theta} \sim t_{(2\alpha)},$$

which, upon rearranging terms, produces an analytical draw from  $p(y_j | \mathbf{y}_{1:j-1}, \boldsymbol{\theta})$ .

### S3. AUTOCORRELATION OF THE GLE INCREMENTS

For the GLE model

$$\int_{-\infty}^t \gamma_K(t-s)V(s) ds = \sqrt{k_B T} F_t, \quad \gamma_K(t) = \frac{\eta}{K} \sum_{k=1}^K \exp(-|t| (k/K)^\rho / \tau_1),$$

McKinley et al. (2009) have shown that the displacement process  $X(t) = \int_0^t V(s) ds$  can be expressed as a linear combination of a Brownian motion  $B(t)$  and  $K-1$  Ornstein-Uhlenbeck processes  $Y_j(t)$ , all independent of each other. That is, let  $\alpha_k = (k/K)^\rho / \tau_1$ ,  $p(y) = \prod_{k=1}^K (y - \alpha_k)$ , and  $r_1, \dots, r_{K-1}$  be the roots of  $p'(y)$ . Then

$$X(t) = \sqrt{\frac{2k_B T}{\eta}} \left( C_0 B(t) + \sum_{j=1}^{K-1} C_j Y_j(t) \right),$$

where  $C_0 = \left( \sum_{k=1}^K \alpha_k^{-1} \right)^{-1/2}$ ,

$$C_j = \frac{1}{r_j} \times \frac{\sqrt{\sum_{k=1}^K \frac{\alpha_k}{(\alpha_k - r_j)^2}}}{\left( \sum_{k=1}^K \frac{1}{\alpha_k - r_j} \right)^2 - \sum_{k=1}^K \frac{1}{(\alpha_k - r_j)^2}},$$

and

$$dX_j(t) = -r_j X_j(t) dt + dB_j(t),$$

with  $B(t)$  and the  $B_j(t)$  all being independent Brownian motions. Using this, the autocorrelation of the incrementes  $\mathbf{x} = (x_1, \dots, x_N)$ ,  $x_n = X(\Delta t \cdot n) - X(\Delta t \cdot (n-1))$  can be calculated analytically:

$$(S7) \quad \text{cov}(x_i, x_j) = \frac{2k_B T}{\eta} \left( C_0^2 \Delta t \delta(k) + \sum_{j=1}^{K-1} \frac{C_j^2}{2r_j} \left( 2e^{-r_j |k|\Delta t} - e^{-r_j |k-1|\Delta t} - e^{-r_j |k+1|\Delta t} \right) \right),$$

where  $k = |i-j|$  and  $\delta(k)$  is the Dirac  $\delta$ -function.

#### S4. SENSITIVITY OF INFERENCE TO UNCERTAINTY ABOUT MEASUREMENT ERROR

To illustrate the impact of uncertainty in the specification of the measurement error, we devised the following simulation based of the first dataset DS-1 in Figure 2. The fitted parameters for the fBM model to DS-1 were  $\mu = -.03$ ,  $\sigma = .25$ , and  $H = .34$ . We used these parameters to simulate a new dataset, DS-1sim. Figure S1(a) displays the posterior parameter densities for DS-1sim with (i) a zero-error model (blue curve), and (ii) the additive error model (16),

$$y_n = x_n + \epsilon_n, \quad \epsilon_n \stackrel{\text{iid}}{\sim} \mathcal{N}(0, \nu^2),$$

with unknown  $\nu$  (red curve) an noninformative prior

$$\pi(\mu, \sigma, H, \nu) \propto 1/(\sigma\nu).$$

The noninformative prior specification for the unknown magnitude  $\nu$  absorbs much of the vari-

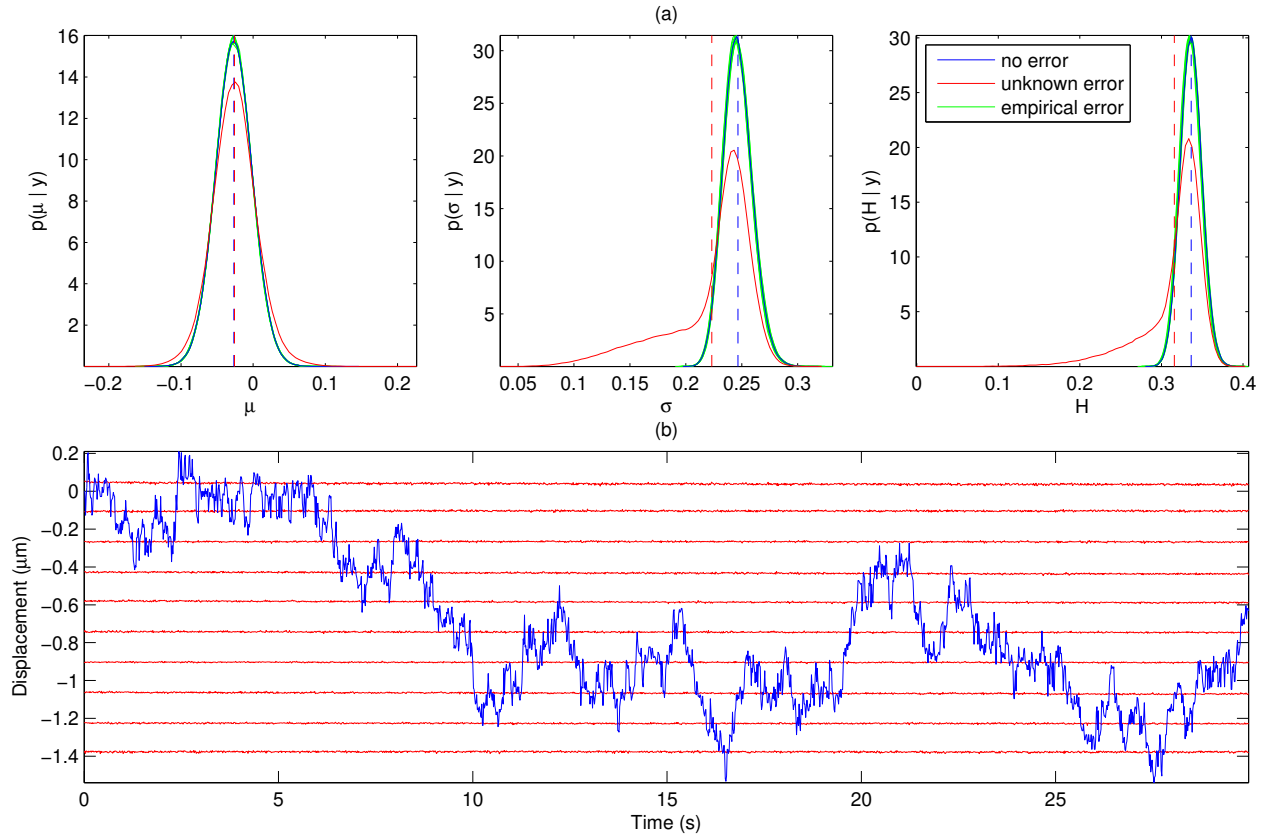


FIGURE S1. (a) Posterior parameter estimates for the fBM model with dataset DS-1sim under various error specifications: no error, unknown error, and with added empirical error but assuming the model is error-free. (b) Comparison of ten pure error displacement curves (red) to signal + error measurement of DS-1.

ability from the actual “signal” into the noise (lower  $\sigma$ ). Filtering out the white noise enhances the non-white components of the residual signal – in this case, it is the long-range (negative) memory  $H$ , which increases the posterior probability of highly subdiffusive models (lower  $\alpha = 2H$ ).

In contrast, ten stuck bead trajectories (pure measurement error) are superimposed onto the trajectory of DS-1 (the real dataset) in Figure S1(b). We see that the measurement error is several orders of magnitude smaller than the observed signal. Indeed, each of these 10 error curves was then added to DS-1<sub>sim</sub> before refitting the fBM model with zero measurement error. Figure S1(a) displays the posterior densities for each parameter and each of the 10 synthetic datasets with added “empirical” error in green. These posterior estimates are almost identical to those with the error-free dataset DS-1<sub>sim</sub> alone. Having observed the same effect of error uncertainty in the GLE model and with several other datasets (both real and simulated), we proceed with our analysis under the assumption that measurement error in these experiments is effectively zero.

### S5. SENSITIVITY OF BAYESIAN MODEL SELECTION TO THE CHOICE OF PRIOR

To illustrate this problem in our particular setting, we simulated 10 datasets from the posterior predictive distribution for the fBM and GLE-200 models based on the analysis of DS-1,

$$p_{\text{pred}}(\mathbf{x} | M_i) = \int p(\mathbf{x} | \boldsymbol{\theta}_i, M_i) \pi_{\text{DS-1}}(\boldsymbol{\theta}_i | M_i) d\boldsymbol{\theta}_i,$$

where

$$\pi_{\text{DS-1}}(\boldsymbol{\theta}_i | M_i) = p(\boldsymbol{\theta}_i | \mathbf{x}_{\text{DS-1}}, M_i) \propto L(\boldsymbol{\theta}_i | \mathbf{x}_{\text{DS-1}}, M_i) \pi(\boldsymbol{\theta}_i | M_i),$$

with the priors (11) and (14) used for model fitting in Section 3. Subsequently, we computed the posterior model probabilities  $p(M_i | \mathbf{x}_{\text{sim}})$  for each dataset  $\mathbf{x}_{\text{sim}}$  using proper priors at two opposing extremes:

1. A noninformative but proper prior  $\pi_{\text{NI}}(\boldsymbol{\theta}_i | M_i)$ , chosen to closely resemble the improper priors used to obtain the posterior predictive distributions. These were of the conjugate forms (11) and (14), with  $\alpha = \beta = 10^{-20}$ ,  $\Omega_H = 0.001$ , and  $\rho \sim \mathcal{N}(0, 1000)$ .
2. The overly-informative prior implied by the *posterior Bayes factor* of Aitkin (1991) which “uses the data twice”. That is, for each simulated dataset  $\mathbf{x}_{\text{sim}}$ , the models were first fit with the improper conjugate priors  $\pi(\boldsymbol{\theta}_i | M_i)$  from (11) and (14). The resulting posterior distributions

$$p(\boldsymbol{\theta}_i | \mathbf{x}_{\text{sim}}, M_i) \propto p(\mathbf{x}_{\text{sim}} | \boldsymbol{\theta}_i, M_i) \pi_i(\boldsymbol{\theta}_i | M_i)$$

were then used as a new prior to *refit* the data, such that we have

$$\begin{aligned} f_i(\mathbf{x}_{\text{sim}}) &= \int p(\mathbf{x}_{\text{sim}} | \boldsymbol{\theta}_i, M_i) p(\boldsymbol{\theta}_i | \mathbf{x}_{\text{sim}}, M_i) d\boldsymbol{\theta}_i \\ &= \frac{\int p(\mathbf{x}_{\text{sim}} | \boldsymbol{\theta}_i, M_i)^2 \pi_i(\boldsymbol{\theta}_i, M_i) d\boldsymbol{\theta}_i}{\int p(\mathbf{x}_{\text{sim}} | \boldsymbol{\theta}_i, M_i) \pi_i(\boldsymbol{\theta}_i | M_i) d\boldsymbol{\theta}_i}. \end{aligned}$$

Figure S2 displays the posterior probabilities for each of the 20 simulated datasets. Both priors above clearly fail to separate the two models but for different reasons. The poor performance of the noninformative prior is a consequence of Lindley’s paradox (Lindley, 1957). Failure of the “double data” prior of (Aitkin, 1991) is due to such a prior favoring the model with a more parcimonious principal components representation. That is, if the data is not used “twice” but

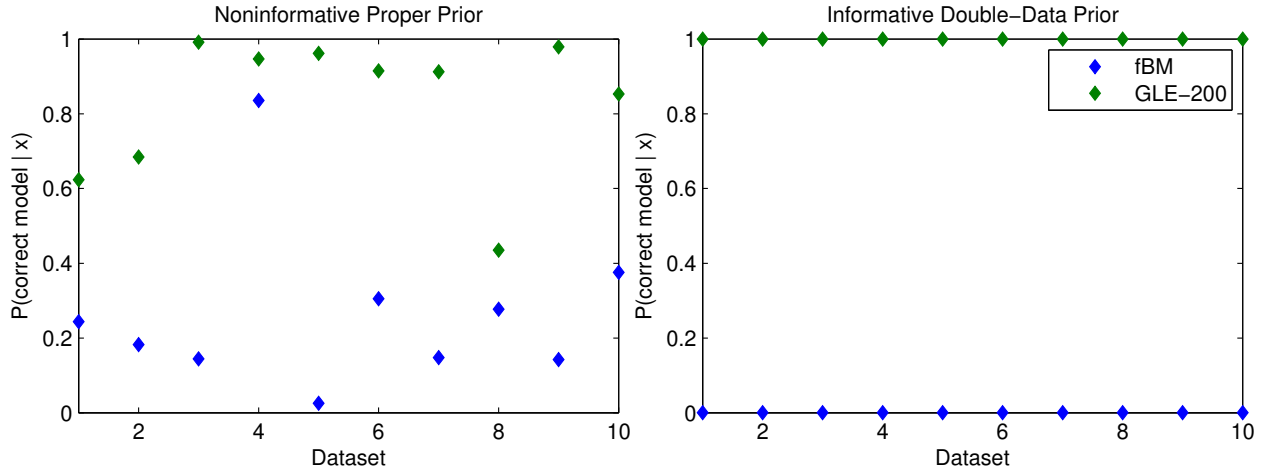


FIGURE S2. Posterior probability of picking the correct model for simulated fBM and GLE-200 datasets for two poor choices of prior.

“ $m$  times”, as  $m \rightarrow \infty$  the posterior Bayes factor of (Aitkin, 1991) reduces to the generalized likelihood ratio

$$\frac{p(\mathbf{x}_{\text{sim}} | \hat{\boldsymbol{\theta}}_1, M_1)}{p(\mathbf{x}_{\text{sim}} | \hat{\boldsymbol{\theta}}_2, M_2)},$$

where  $\hat{\boldsymbol{\theta}}_i$  are the MLEs of  $\boldsymbol{\theta}_i$  under each model. The log-densities  $\log(p(\mathbf{x}_{\text{sim}} | \hat{\boldsymbol{\theta}}_i, M_i))$  each consist of a sum of squared residuals and a log-determinant. Our experiments suggest that the residuals for the fBM and GLE-200 models with  $\boldsymbol{\theta}_i = \hat{\boldsymbol{\theta}}_i$  are virtually the same. However, for any fixed number of modes, the GLE model is asymptotically *diffusive*. Thus, while fBM increments have power law decay, the GLE-200 increments have power law intermediate behavior but exponential decay. This translates to more sharply decaying eigenvalues of the corresponding variance matrix, and thus smaller log-determinant penalty. It is for this reason that the double data prior emphatically favors the GLE-200 model, even for data simulated under fBM.

#### REFERENCES

- Aitkin, M. (1991). Posterior Bayes factors. *Journal of the Royal Statistical Society. Series B (Methodological)*, 53(1): 111–142.
- Andrews, D.W.K. and Sun, Y. (2004). Adaptive local polynomial Whittle estimation of long-range dependence. *Econometrica*, 72(2): 569–614.
- Baczkowski, A.D. and Bond, S.D. (2013). Numerical integration of the extended variable generalized Langevin equation with a positive Prony representable memory kernel. *The Journal of Chemical Physics*, 139(4): 044107.
- Berger, J.O. and Pericchi, L.R. (1996). The intrinsic Bayes factor for model selection and prediction. *Journal of the American Statistical Association*, 91(433): 109–122.
- Brockwell, P.J. and Davis, R.A. (2009). *Time Series: Theory and Methods*. Springer, New York.

- Bronstein, I., Israel, Y., Kepten, E., Mai, S., Shav-Tal, Y., Barkai, E., and Garini, Y. (2009). Transient Anomalous Diffusion of Telomeres in the Nucleus of Mammalian Cells. *Physical Review Letters*, 103(1): 018102 1–4.
- Burov, S., Jeon, J.H., Metzler, R., and Barkai, E. (2011). Single particle tracking in systems showing anomalous diffusion: the role of weak ergodicity breaking. *Physical Chemistry Chemical Physics*, 13(5): 1800–1812.
- Carlstedt, I., Lindgren, H., and Sheehan, J. (1983a). The macromolecular structure of human cervical-mucus glycoproteins. studies on fragments obtained after reduction of disulphide bridges and after subsequent trypsin digestion. *Biochem. J*, 213: 427–435.
- Carlstedt, I., Lindgren, H., Sheehan, J., Ulmsten, U., and Wingerup, L. (1983b). Isolation and characterization of human cervical-mucus glycoproteins. *Biochem. J*, 211: 13–22.
- Carlstedt, I., Sheehan, J., Ulmsten, U., and Wingerup, L. (1982). Isolation and purification of the mucin component of human cervical mucus. In *Mucus in Health and Disease II*, pages 273–275. Springer.
- Carlstedt, I. and Sheehan, J.K. (1984). Macromolecular properties and polymeric structure of mucus glycoproteins. *Mucus and mucosa*, pages 157–172.
- Caspi, A. and Granek, R. (2000). Enhanced diffusion in active intracellular transport. *Physical Review Letters*, 85: 5655–5658.
- Cone, R.A. (2009). Barrier properties of mucus. *Advanced Drug Delivery Reviews*, 61(2): 75–85.
- Córdoba, A., Indei, T., and Schieber, J.D. (2012). Elimination of inertia from a Generalized Langevin Equation: Applications to microbead rheology modeling and data analysis. *Journal of Rheology (1978-present)*, 56(1): 185–212.
- Dawson, M., Wirtz, D., and Hanes, J. (2003). Enhanced viscoelasticity of human cystic fibrotic sputum correlates with increasing microheterogeneity in particle transport. *Journal of Biological Chemistry*, 278(50): 50393–50401.
- Didier, G., McKinley, S.A., Hill, D.B., and Fricks, J. (2012). Statistical challenges in microrheology. *Journal of Time Series Analysis*, 33(5): 724–743.
- Ensign, L.M., Tang, B.C., Wang, Y.Y., Terence, A.T., Hoen, T., Cone, R., and Hanes, J. (2012). Mucus-penetrating nanoparticles for vaginal drug delivery protect against herpes simplex virus. *Science translational medicine*, 4(138): 138ra79–138ra79.
- Ernst, D., Hellmann, M., Köhler, J., and Weiss, M. (2012). Fractional Brownian motion in crowded fluids. *Soft Matter*, 8(18): 4886–4889.
- Ferry, J.D. (1980). *Viscoelastic properties of polymers*. John Wiley & Sons.
- Fricks, J., Yao, L., Elston, T.C., and Forest, M.G. (2009). Time-domain methods for diffusive transport in soft matter. *SIAM Journal on Applied Mathematics*, 69(5): 1277–1308.
- Georgiades, P., Pudney, P.D.A., Thornton, D.J., and Waigh, T.A. (2014). Particle tracking microrheology of purified gastrointestinal mucins. *Biopolymers*, 101(4): 366–377.

- Ghoreishy, M.H.R. (2012). Determination of the parameters of the prony series in hyper-viscoelastic material models using the finite element method. *Materials & Design*, 35: 791–797.
- Golding, I. and Cox, E. (2006). Physical Nature of Bacterial Cytoplasm. *Physical Review Letters*, 96(9): 098102.
- Green, P.J. (1995). Reversible jump Markov chain Monte Carlo computation and Bayesian model determination. *Biometrika*, 82(4): 711–732.
- Hauge, E.H. and Martin-Löf, A. (1973). Fluctuating hydrodynamics and Brownian motion. *Journal of Statistical Physics*, 7(3): 259–281.
- Hill, D.B., Vasquez, P.A., Mellnik, J., McKinley, S.A., Vose, A., Mu, F., Henderson, A.G., Donaldson, S.H., Alexis, N.E., Boucher, R.C., and Forest, M.G. (2014). A Biophysical Basis for Mucus Solids Concentration as a Candidate Biomarker for Airways Disease. *PLoS ONE*, 9(2): e87681.
- Indei, T., Schieber, J.D., Córdoba, A., and Pilyugina, E. (2012). Treating Inertia in Passive Microbead Rheology. *Physical Review E*, 85(2): 021504 1–18.
- Jeffreys, H. (1961). *The Theory of Probability*. Oxford University Press, New York.
- Jeon, J.H. and Metzler, R. (2010). Analysis of short subdiffusive time series: scatter of the time-averaged mean-squared displacement. *Journal of Physics A: Mathematical and Theoretical*, 43(25): 252001.
- Jeon, J.H., Tejedor, V., Burov, S., Barkai, E., Selhuber-Unkel, C., Berg-Sørensen, K., Oddershede, L., and Metzler, R. (2011). In Vivo Anomalous Diffusion and Weak Ergodicity Breaking of Lipid Granules. *Physical Review Letters*, 106(4): 048103.
- Kass, R.E. and Raftery, A.E. (1995). Bayes factors. *Journal of the American Statistical Association*, 90(430): 773–795.
- Kim, C.J. and Nelson, C.R. (1999). *State-space models with regime switching*. MIT Press, Cambridge, MA.
- Kneller, G.R. (2011). Generalized Kubo relations and conditions for anomalous diffusion: Physical insights from a mathematical theorem. *The Journal of Chemical Physics*, 134(22): 224106.
- Kou, S.C. (2008). Stochastic modeling in nanoscale biophysics: Subdiffusion within proteins. *The Annals of Applied Statistics*, 2(2): 501–535.
- Kou, S.C. and Xie, X.S. (2004). Generalized Langevin equation with fractional Gaussian noise: Subdiffusion within a single protein molecule. *Physical Review Letters*, 93(18): 180603 1–4.
- Kubo, R. (1966). The fluctuation-dissipation theorem. *Reports on Progress in Physics*, 29: 255–284.
- Kupferman, R. (2004). Fractional kinetics in Kac-Zwanzig heat bath models. *Journal of Statistical Physics*, 114(1-2): 291–326.
- Lai, B.E., Henderson, M.H., Peters, J.J., Walmer, D.K., and Katz, D.F. (2009). Transport Theory for HIV Diffusion through In Vivo Distributions of Topical Microbicide Gels. *Biophysical Journal*, 97(9): 2379–2387.
- Lai, S.K., O’Hanlon, D.E., Harrold, S., Man, S.T., Wang, Y.Y., Cone, R., and Hanes, J. (2007). Rapid transport of large polymeric nanoparticles in fresh undiluted human mucus. *Proceedings of the*

- National Academy of Sciences of the United States of America*, 104(5): 1482–1487.
- Lartillot, N. and Philippe, H. (2006). Computing Bayes factors using thermodynamic integration. *Systematic Biology*, 55(2): 195–207.
- Li, W.L.S. and Drummond, A.J. (2012). Model averaging and Bayes factor calculation of relaxed molecular clocks in Bayesian phylogenetics. *Molecular Biology and Evolution*, 29(2): 751–761.
- Lindley, D.V. (1957). A statistical paradox. *Biometrika*, 44(1-2): 187–192.
- Lubelski, A., Sokolov, I.M., and Klafter, J. (2008). Nonergodicity mimics inhomogeneity in single particle tracking. *Physical Review Letters*, 100(25): 250602.
- Lunn, D., Barrett, J., Sweeting, M., and Thompson, S. (2013). Fully bayesian hierarchical modelling in two stages, with application to meta-analysis. *Journal of the Royal Statistical Society: Series C*, 62(4): 551–572.
- Magdziarz, M. and Klafter, J. (2010). Detecting origins of subdiffusion: P-variation test for confined systems. *Physical Review E*, 82(1 Pt 1): 011129.
- Magdziarz, M., Weron, A., and Burnecki, K. (2009). Fractional Brownian Motion Versus the Continuous-Time Random Walk: A Simple Test for Subdiffusive Dynamics. *Physical review letters*, 103(18): 180602.
- Mandelbrot, B.B. and Van Ness, J.W. (1968). Fractional Brownian motions, fractional noises and applications. *SIAM Review*, 10(4): 422–437.
- Mason, T.G. and Weitz, D.A. (1995). Optical measurements of frequency-dependent linear viscoelastic moduli of complex fluids. *Physical Review Letters*, 74(7): 1250–1253.
- McKinley, S.A. (2009). Anomalous diffusion of distinguished particles in bead-spring networks. Available at <http://arxiv.org/pdf/0911.4293v1.pdf>.
- McKinley, S.A., Yao, L., and Forest, M.G. (2009). Transient anomalous diffusion of tracer particles in soft matter. *Journal of Rheology*, 53: 1487 – 1506.
- Meroz, Y., Sokolov, I., and Klafter, J. (2013). Test for Determining a Subdiffusive Model in Ergodic Systems from Single Trajectories. *Physical review letters*, 110(9): 090601.
- Meroz, Y., Sokolov, I.M., and Klafter, J. (2011). Unequal Twins: Probability Distributions Do Not Determine Everything. *Physical Review Letters*, 107(26): 260601.
- Metzler, R. and Klafter, J. (2000). The random walk's guide to anomalous diffusion: a fractional dynamics approach. *Physics Reports*, 339(1): 1–77.
- Metzler, R., Tejedor, V., Jeon, J., He, Y., Deng, W., Burov, S., and Barkai, E. (2009). Analysis of single particle trajectories: From normal to anomalous diffusion. *Acta Physica Polonica B*, 40(5): 1315.
- Monnier, N., Guo, S.M., Mori, M., He, J., Lénárt, P., and Bathe, M. (2012). Bayesian approach to msd-based analysis of particle motion in live cells. *Biophysical Journal*, 103: 616 – 626.
- Morgado, R., Oliveira, F., Batrouni, G., and Hansen, A. (2002). Relation between Anomalous and Normal Diffusion in Systems with Memory. *Physical Review Letters*, 89(10): 100601 1–4.

- Olmsted, S., Padgett, J., Yudin, A., Whaley, K., Moench, T., and Cone, R. (2001). Diffusion of macromolecules and virus-like particles in human cervical mucus. *Biophysj*, 81(4): 1930–1937.
- O'Malley, D., Cushman, J.H., and Johnson, G. (2011). Scaling laws for fractional Brownian motion with power-law clock. *Journal of Statistical Mechanics: Theory and Experiment*, 2011(01): L01001.
- Ottobre, M. and Pavliotis, G. (2011). Asymptotic analysis for the generalized langevin equation. *Nonlinearity*, 24(5): 1629.
- Park, S.W. and Schapery, R.A. (1999). Methods of interconversion between linear viscoelastic material functions. part ia numerical method based on prony series. *International Journal of Solids and Structures*, 36(11): 1653–1675.
- Rangarajan, G. and Ding, M. (2000). Anomalous diffusion and the first passage time problem. *Physical Review E*, 62(1): 120–133.
- Robert, C.P., Cornuet, J.M., Marin, J.M., and Pillai, N.S. (2011). Lack of confidence in approximate bayesian computation model choice. *Proceedings of the National Academy of Sciences*, 108(37): 15112–15117.
- Robinson, P.M. (1995). Gaussian semiparametric estimation of long range dependence. *The Annals of Statistics*, 23(5): 1630–1661.
- Rosenblatt, M. (1952). Remarks on a multivariate transformation. *Ann. Math. Statist.*, 23(3): 470 – 472.
- Rouse, P.E. (1953). A theory of the linear viscoelastic properties of dilute solutions of coiling polymers. *The Journal of Chemical Physics*, 21(7): 1272–1280.
- Rubinstein, M. and Colby, R.H. (2003). *Polymer Physics*. Oxford University Press, New York.
- Saltzman, W.M., Radomsky, M.L., Whaley, K., and Cone, R. (1994). Antibody diffusion in human cervical mucus. *Biophysical Journal*, 66(2): 508–515.
- Saxton, M. (2007). A biological interpretation of transient anomalous subdiffusion. I. Qualitative model. *Biophysical Journal*, 92(4): 1178–1191.
- Schink, H.M., Slot, J.J.M., Jongschaap, R.J.J., and Mellema, J. (2000). The rheology of systems containing rigid spheres suspended in both viscous and viscoelastic media, studied by Stokesian dynamics simulations. *Journal of Rheology (1978-present)*, 44(3): 473–498.
- Seisenberger, G., Ried, M.U., Endress, T., Büning, H., Hallek, M., and Bräuchle, C. (2001). Real-time single-molecule imaging of the infection pathway of an adeno-associated virus. *Science*, 294(5548): 1929.
- Selhuber-Unkel, C., Yde, P., Berg-Sørensen, K., and Oddershede, L.B. (2009). Variety in intracellular diffusion during the cell cycle. *Physical Biology*, 6(2): 025015.
- Soussou, J.E., Moavenzadeh, F., and Gradowczyk, M.H. (1970). Application of prony series to linear viscoelasticity. *Transactions of The Society of Rheology*, 14(4): 573–584.
- Squires, T.M. and Mason, T.G. (2010). Fluid Mechanics of Microrheology. *Annual Review of Fluid Mechanics*, 42(1): 413–438.

- Suk, J.S., Lai, S.K., Wang, Y.Y., Ensign, L.M., Zeitlin, P.L., Boyle, M.P., and Hanes, J. (2009). The penetration of fresh undiluted sputum expectorated by cystic fibrosis patients by non-adhesive polymer nanoparticles. *Biomaterials*, 30(13): 2591–2597.
- Suk, J.S., Suh, J., Lai, S.K., and Hanes, J. (2007). Quantifying the intracellular transport of viral and nonviral gene vectors in primary neurons. *Experimental Biology and Medicine*, 232(3): 461–469.
- Szymanski, J. and Weiss, M. (2009). Elucidating the origin of anomalous diffusion in crowded fluids. *Physical Review Letters*, 103(3): 38102.
- Tejedor, V., Bénichou, O., Voituriez, R., Jungmann, R., Simmel, F., Selhuber-Unkel, C., Oddershede, L.B., and Metzler, R. (2010). Quantitative Analysis of Single Particle Trajectories: Mean Maximal Excursion Method. *Biophysical Journal*, 98(7): 1364–1372.
- Thornton, D.J. and Sheehan, J.K. (2004). From mucins to mucus: toward a more coherent understanding of this essential barrier. *Proceedings of the American Thoracic Society*, 1(1): 54–61.
- Tolić-Nørrelykke, I., Munteanu, E.L., Thon, G., Oddershede, L., and Berg-Sørensen, K. (2004). Anomalous Diffusion in Living Yeast Cells. *Physical Review Letters*, 93(7): 078102.
- Toni, T., Welch, D., Strelkowa, N., Ipsen, A., and Stumpf, M.P.H. (2009). Approximate Bayesian computation scheme for parameter inference and model selection in dynamical systems. *Journal of the Royal Society Interface*, 6(31): 187–202.
- Valentine, M., Kaplan, P., Thota, D., Crocker, J., Gisler, T., Prud'homme, R., Beck, M., and Weitz, D. (2001). Investigating the microenvironments of inhomogeneous soft materials with multiple particle tracking. *Physical Review E*, 64(6): 061506 1–9.
- Vanpaemel, W. (2010). Prior sensitivity in theory testing: An apologia for the bayes factor. *Journal of Mathematical Psychology*, 54(6): 491–498.
- Vysheirsky, V. and Girolami, M.A. (2008). Bayesian ranking of biochemical system models. *Bioinformatics*, 24(6): 833–839.
- Whaley, K.J., Hanes, J., Shattock, R., Cone, R.A., and Friend, D.R. (2010). Novel approaches to vaginal delivery and safety of microbicides: biopharmaceuticals, nanoparticles, and vaccines. *Antiviral research*, 88: S55–S66.
- Wong, I., Gardel, M., Reichman, D., Weeks, E., Valentine, M., Bausch, A., and Weitz, D. (2004a). Anomalous Diffusion Probes Microstructure Dynamics of Entangled F-Actin Networks. *Physical Review Letters*, 92(17): 178101.
- Wong, I.Y., Gardel, M.L., Reichman, D.R., Weeks, E.R., Valentine, M.T., Bausch, A.R., and Weitz, D.A. (2004b). Anomalous diffusion probes microstructure dynamics of entangled F-actin networks. *Physical review letters*, 92(17): 178101.
- Zwanzig, R. (2001). *Nonequilibrium Statistical Mechanics*. Oxford University Press, New York.
- Zwanzig, R. and Bixon, M. (1970). Hydrodynamic Theory of the Velocity Correlation Function. *Physical Review A*, 2(5): 2005–2012.